

Assessment of a Physics-based Retrieval of Exoplanet Atmospheric Temperatures from Infrared Emission Spectra

Franz Schreier,^{1*} J. Lee Grenfell,² Fabian Wunderlich,² and Thomas Trautmann¹

¹*DLR — Deutsches Zentrum für Luft- und Raumfahrt, Institut für Methodik der Fernerkundung, 82234 Oberpfaffenhofen, Germany*

²*DLR — Deutsches Zentrum für Luft- und Raumfahrt, Institut für Planetenforschung, Rutherfordstr. 2, 12489 Berlin, Germany*

Accepted 2023 May 16. Received 2023 May 15; in original form 2023 February 22

ABSTRACT

Atmospheric temperatures are to be estimated from thermal emission spectra of Earth-like exoplanets orbiting M-stars as observed by current and future planned missions. To this end, a line-by-line radiative transfer code is used to generate synthetic thermal infrared (TIR) observations. The range of “observed” intensities provides a rough hint of the atmospheric temperature range without any a priori knowledge. The equivalent brightness temperature (related to intensities by Planck’s function) at certain wavenumbers can be used to estimate the atmospheric temperature at corresponding altitudes. To exploit the full information provided by the measurement we generalize Chahine’s original approach and infer atmospheric temperatures from all spectral data using the wavenumber-to-altitude mapping defined by the weighting functions. Chahine relaxation allows an iterative refinement of this “first guess”. Analysis of the 4.3 μm and 15 μm carbon dioxide TIR bands enables an estimate of atmospheric temperatures for rocky exoplanets even for low signal to noise ratios of 10 and medium resolution. Inference of Trappist-1e temperatures is, however, more challenging especially for CO₂ dominated atmospheres: the “standard” 4.3 μm and 15 μm regions are optically thick and an extension of the spectral range towards atmospheric window regions is important. If atmospheric composition (essentially CO₂ concentration) is known temperatures can be estimated remarkably well; quality measures such as the residual norm provide hints on incorrect abundances. In conclusion, temperature in the mid atmosphere of Earth-like planets orbiting cooler stars can be quickly estimated from thermal IR emission spectra with moderate resolution.

Key words: Astrobiology – Radiative transfer – Techniques: spectroscopic – Planets and satellites: atmospheres – Infrared: planetary systems; Methods: data analysis

1 INTRODUCTION

A quarter century after the detection of the first planet orbiting a main sequence star (Mayor & Queloz 1995) exoplanetary science has developed astonishingly quickly and is likely to continue on this path (Mérand et al. 2021). Some 5000 exoplanets are known today¹, several dedicated space missions are already in orbit for detection (Kepler/K2, Transiting Exoplanet Survey Satellite (TESS), . . .), and characterisation (CHaracterising ExOPlanet Satellite (CHEOPS, Benz et al. 2018)), and some others are in development, e.g. PLANetary Transits and Oscillations of stars (PLATO, Rauer et al. 2014), Atmospheric Remote-sensing Infrared Exoplanet Large-survey (ARIEL, Tinetti et al. 2018) or the proposed Large Interferometer For Exoplanets (LIFE, Defrère et al. 2018; Quanz et al. 2022a,b; Konrad et al. 2022). The successfully launched James Webb Space Telescope (JWST) with its several infrared (IR) instruments will considerably expand our knowledge for a wide range of exoplanets (Greene et al. 2016).

Atmospheric characterisation by means of microwave, IR, or ultraviolet spectroscopy is performed routinely for Earth as well as for the Solar System planets and moons (Hanel et al. 2003) and its

feasibility has also been demonstrated for extrasolar planets, mostly hot Jupiters (e.g. Madhusudhan & Seager 2009). For atmospheric remote sensing “optimal estimation” (Rodgers 1976, 2000) is by far the most common inversion technique and this Bayesian method has also been used in an exoplanet context, e.g. Irwin et al. (2008); Lee et al. (2012); Barstow et al. (2013, 2016) or more recently Shulyak et al. (2019). Bayesian methods such as optimal estimation (OE) heavily rely on a priori knowledge that is in general readily available for Earth’s atmosphere as well as many Solar System bodies, but which is less well-known for exoplanets. Grid based search methods have become a standard approach for exoplanet characterisation; because of the need to perform millions to billions of radiative transfer forward model runs, sophisticated methods based on Monte Carlo Markov Chains and Nested Sampling are exploited to speed up the search (for recent reviews see e.g. Madhusudhan 2018; Barstow & Heng 2020; MacDonald & Batalha 2023).

Line et al. (2013) have performed an intercomparison of three retrieval codes utilising OE and two Monte Carlo methods and concluded that for good measurements (high spectral resolution and little noise) the estimates agree quite well. More recently, Barstow et al. (2020) compared three retrieval codes CHIMERA (Line et al. 2012), NEMESIS (Irwin et al. 2008), and Tau-REx (Waldmann et al. 2015) and reported mostly consistent results but emphasised the important role of radiative transfer modeling since the same inverse problem

* E-mail: franz.schreier@dlr.de (FS)

¹ <http://exoplanet.eu/>

solver (nested sampling MultiNest, [Feroz et al. 2009](#)) is used by all three codes; hence the testing of additional inverse solvers is desirable. Likewise, the critical impact of the forward model was also emphasised by [Barstow et al. \(2022\)](#) who presented an intercomparison of five codes (ARCIS, [Min et al. 2020](#), NEMESIS, Pyrat BAY, [Cubillos & Bleicic 2021](#), Tau-REx, and POSEIDON, [MacDonald & Madhusudhan 2017](#)).

Pressure, temperature, and molecular concentrations depend on space (and time), and a discretisation is mandatory for numerical analysis. The latitudinal and longitudinal dependencies are largely ignored (for a discussion of 2D or 3D effects on emission and transmission see e.g. [Feng et al. 2016](#); [Bleicic et al. 2017](#); [Taylor et al. 2020](#) and [Caldas et al. 2019](#); [MacDonald et al. 2020](#), respectively; see also [Pluriel 2023](#) for a recent review). Whereas assuming molecular concentrations which are constant in altitude is likely acceptable as a first step, the assumption of isothermal temperature profiles (e.g. [Barstow et al. 2022](#)) is problematic. Layer-by-layer representations (standard for Earth remote sensing) have been criticised as troublesome due to the limited information content ([Line et al. 2013](#); [Parmentier & Guillot 2014](#)), and parameterised representations of the vertical dependence of temperature are quite common (e.g. [Madhusudhan & Seager 2009](#); [von Paris et al. 2013](#); [Morley et al. 2017a](#)). A novel function expansion approach along with a standard nonlinear least squares solver has been studied by [Schreier et al. \(2020\)](#). [Barstow & Heng \(2020\)](#) recommended to “conduct retrievals . . . with a variety of temperature structures and . . . to investigate alternative approaches.”

Here we examine the feasibility of temperature sounding by means of an iterative relaxation developed in the late sixties by [Chahine \(1968, 1970, 1972\)](#) that is presented in several textbooks on atmospheric radiation (e.g. [Goody & Yung 1989](#); [Liou 1980](#); [Hanel et al. 2003](#); [Zdunkowski et al. 2007](#)) but rarely used today. According to “Subsection 6.5.2 — A physical approach to retrieval” in [Goody & Yung \(1989\)](#) it is a “simple idea easy to visualize and to extend to new circumstances” and exploits the properties of the weighting functions (the derivatives of the transmission w.r.t. altitude). Extensions and/or refinements of this approach were presented by [Smith \(1970\)](#) and [Twomey et al. \(1977\)](#). These relaxation methods have been used for analysis of IR and microwave observations of Earth’s atmosphere, and for temperature sounding of Venus (e.g. [Taylor et al. 1980](#)), Mars ([Lellouch et al. 1991a,b](#); [Haus & Titov 2000](#)), and Jupiter ([Gautier et al. 1977, 1979](#)).

The organisation of the paper is as follows: The following section describes our methodology (radiative transfer, Chahine relaxation, . . .) along with the code and data. We demonstrate the feasibility to estimate the temperature for Earth-like exoplanets in Section 3: Computationally fast estimates exploiting a “mapping” of the wavenumber space to the altitude space as well as iterative refinements based on a comparison of observed and model spectra are presented. We continue with a discussion in Section 4 and give our conclusions in Section 5.

2 THEORY

2.1 Forward model — infrared radiative transfer

In a gaseous atmosphere with local thermodynamic equilibrium the upwelling intensity (radiance) I at wavenumber ν is described by the Schwarzschild equation of radiative transfer ([Goody & Yung 1989](#);

[Hanel et al. 2003](#))

$$I(\nu) = \mathcal{T}(\nu, 0) B(\nu, T_{\text{surf}}) + \int_0^{\tau(\nu, z)} B(\nu, T(\tau')) \exp(-\tau'(\nu)) d\tau' \quad (1)$$

$$= \mathcal{T}(\nu, 0) B(\nu, T_{\text{surf}}) - \int_0^\infty B(\nu, T(z')) \frac{\partial \mathcal{T}(\nu, z')}{\partial z'} dz' \quad (2)$$

where $B = 2hc^2\nu^3 / [\exp(hc\nu/k_B T) - 1]$ is Planck’s function at temperature T (h , c , k_B are the Planck constant, speed of light, and Boltzmann constant, respectively). For the surface contribution $I_{\text{surf}}(\nu) \equiv \mathcal{T}(\nu, 0) B(\nu, T_{\text{surf}})$ we assume a Planck black body emission attenuated by the intermediate atmosphere and a temperature identical to the bottom of the atmosphere (BoA) temperature, i.e. $T_{\text{surf}} = T_{\text{BoA}} = T(z=0)$.

The monochromatic transmission \mathcal{T} , closely related to the optical depth τ , between observer and altitude z is given by Beer’s law

$$\mathcal{T}(\nu, z) = \exp(-\tau(\nu, z)) \quad (3)$$

$$= \exp\left[-\int_z^\infty \sum_m k_m(\nu, p(z'), T(z')) n_m(z') dz'\right],$$

with n_m the density of molecule m , and k_m the pressure and temperature dependent absorption cross section obtained by summing over the contributions from many lines. For simplicity a vertical path is assumed; for a slant path with angle θ in a plane-parallel atmosphere replace $z' \rightarrow z'/\cos(\theta)$. The finite spectral resolution of the instrument is taken into account by convolution of the monochromatic intensity (1) (or transmission (3)) with a spectral response function (SRF, e.g. Gaussian).

The upper atmosphere has a low abundance of absorbers and is therefore almost transparent (i.e., transmission close to one); with an increasingly longer atmospheric path (decreasing z) attenuation becomes stronger especially at wavenumbers with strong absorption in the band or line center (Fig. 1 top-right). Here path length s refers to the distance to the observer, essentially at “infinity”, in practice at top-of-atmosphere (ToA), and is linked to altitude via $s = z_{\text{ToA}} - z$, cf. Eq. (3). Viewed as a function of altitude the transmission decays rapidly to zero for these wavenumbers (Fig. 1 top-left), i.e. photons from the lower atmosphere cannot penetrate to space and the ToA radiation arises mainly from the upper atmospheric layers. The so-called weighting function,² the partial derivative $K(\nu, z) \equiv \partial \mathcal{T}(\nu, z)/\partial z$ in (2), quantifies the dominant contribution (or weight) of an altitude layer to the outgoing radiation (Fig. 1 bottom panels, see also [Liou \(1980, Fig. 7.6\)](#), [Goody & Yung \(1989, Fig. 6.17\)](#), and [Hanel et al. \(2003, Fig. 8.2.1\)](#)). Note that the weighting function is similar, but not identical to the temperature Jacobian $\partial I(\nu)/\partial T(z)$ that measures the radiation’s sensitivity to changes of temperature (see [Schreier et al. 2020, Fig. 10](#)). Both the weighting functions and the Jacobian clearly demonstrate that the radiation carries little information of the lowermost and upper atmospheric layers.

² A note on terminology: different terms are used for the derivative $\partial \mathcal{T}/\partial z$: weighting functions [Liou \(1980\)](#); [Hanel et al. \(2003\)](#); [Zdunkowski et al. \(2007\)](#), kernel functions [Goody & Yung \(1989\)](#), or contribution functions. Moreover, “Jacobian” and “weighting function” are often used interchangeably; however, for temperature retrievals using nonlinear least squares the Jacobian is the partial derivative of the radiance w.r.t. the state vector \vec{x} , $\partial I/\partial \vec{x}$, where \vec{x} is a discrete representation of the temperature profile.

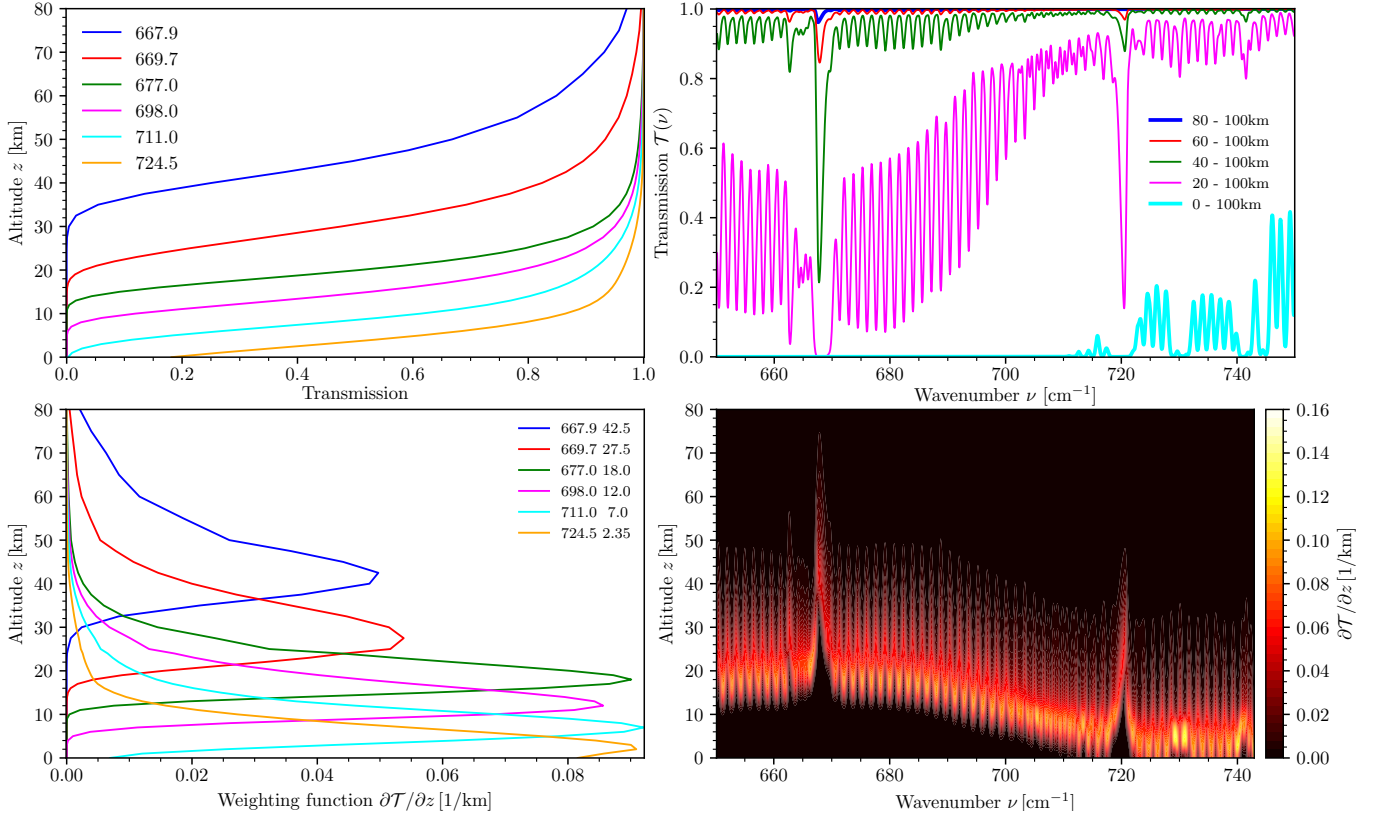


Figure 1. Transmission and weighting functions in the longwave TIR ($\text{CO}_2 \nu_2$ band at $15 \mu\text{m}$, nadir view, Earth’s midlatitude summer (MLS) atmosphere (Anderson et al. 1986), Gaussian response function of half width $\Gamma = 0.25 \text{ cm}^{-1}$ corresponding to a resolution $R \approx 2800$). The upper panels show the transmission as a function of wavenumber for several atmospheric paths (right) and transmission vs. altitude (related to path length $s = z_{\text{ToA}} - z$) for selected wavenumbers (left). The lower panel shows individual weighting functions for selected wavenumbers (left) and a contour plot. Numbers in the left legends indicate the wavenumber [cm^{-1}] and the corresponding peak altitude [km] (bottom-left).

2.2 Inversion — Chahine relaxation

According to Rodgers (1976) “the intensity to be measured is . . . a weighted mean of the Planck function profile with the weighting function”. The bell-shape of the weighting function (Fig. 1 bottom-left) can be exploited for analysis of TIR spectra. Assuming a delta-function-like weighting function the Schwarzschild equation (1) reduces (Hanel et al. 2003) to

$$I(\tilde{\nu}) \approx I_{\text{surf}}(\tilde{\nu}) + B(\tilde{\nu}, T(\tilde{z}_\nu)) \quad (4)$$

with \tilde{z}_ν the altitude where $K(\nu, z)$ has a maximum for a given ν . A first approximation of the atmospheric temperature can thus be inferred from the observed Equivalent Brightness Temperature (EBT), i.e.

$$\begin{aligned} T(\tilde{z}_\nu) \approx T_B(\tilde{\nu}) &\equiv B^{-1}\left(I_{\text{obs}}(\tilde{\nu}) - I_{\text{surf}}(\tilde{\nu})\right) \\ &= \frac{hc\tilde{\nu}/k_B}{\log\left(2hc^2\tilde{\nu}^3 / (I_{\text{obs}}(\tilde{\nu}) - I_{\text{surf}}(\tilde{\nu}))\right)} \end{aligned} \quad (5)$$

This estimate can be iteratively improved using a relaxation scheme originally proposed by Chahine (1968, 1970)

$$T_{i+1}(\tilde{z}_\nu) \approx B^{-1}\left(\frac{I_{\text{obs}}(\tilde{\nu}) - I_{\text{surf}}(\tilde{\nu})}{I_{\text{mod}}(\tilde{\nu}, T_i) - I_{\text{surf}}(\tilde{\nu})} B(\tilde{\nu}, T_i(\tilde{z}_\nu))\right) \quad (6)$$

where T_i denotes the temperature for iteration i and $I_{\text{mod}}(\tilde{\nu}, T_i)$ the corresponding modelled radiance according to (1).

2.3 Implementation

For our forward model we use Python for Computational Atmospheric Spectroscopy (Py4CATS, Schreier et al. 2019, available at <https://atmos.eoc.dlr.de/tools/py4cats/>), a Python re-implementation of the Generic Atmospheric Radiation Line-by-line Infrared Code (Schreier et al. 2014). GARLIC has been thoroughly verified by intercomparison with other codes (e.g. Schreier et al. 2018b) and validated by comparison to effective height spectra (Schreier et al. 2018a) generated from Earth observations of the Atmospheric Chemistry Experiment — Fourier transform spectrometer (ACE-FTS, Bernath 2017).

Py4CATS and GARLIC compute molecular absorption cross sections k_m assuming a (default) Voigt line shape (Schreier 2018), where the wavenumber grid point spacing is adjusted automatically for each molecule, pressure and temperature to a fraction of the typical line width. Next, cross sections scaled by molecular number densities are summed up to absorption coefficients; then standard quadrature schemes are used to compute optical depths and radiances. Both observed and modelled spectra are convolved with a Gaussian spectral response function of constant width (with a default sampling of 4 points per half width at half maximum (HWHM)). Py4CATS makes heavy use of Numpy (van der Walt et al. 2011; Harris et al. 2020) (and occasionally SciPy (Virtanen et al. 2020) and Matplotlib (Hunter 2007)).

The synthetic measurement spectrum is generated by adding

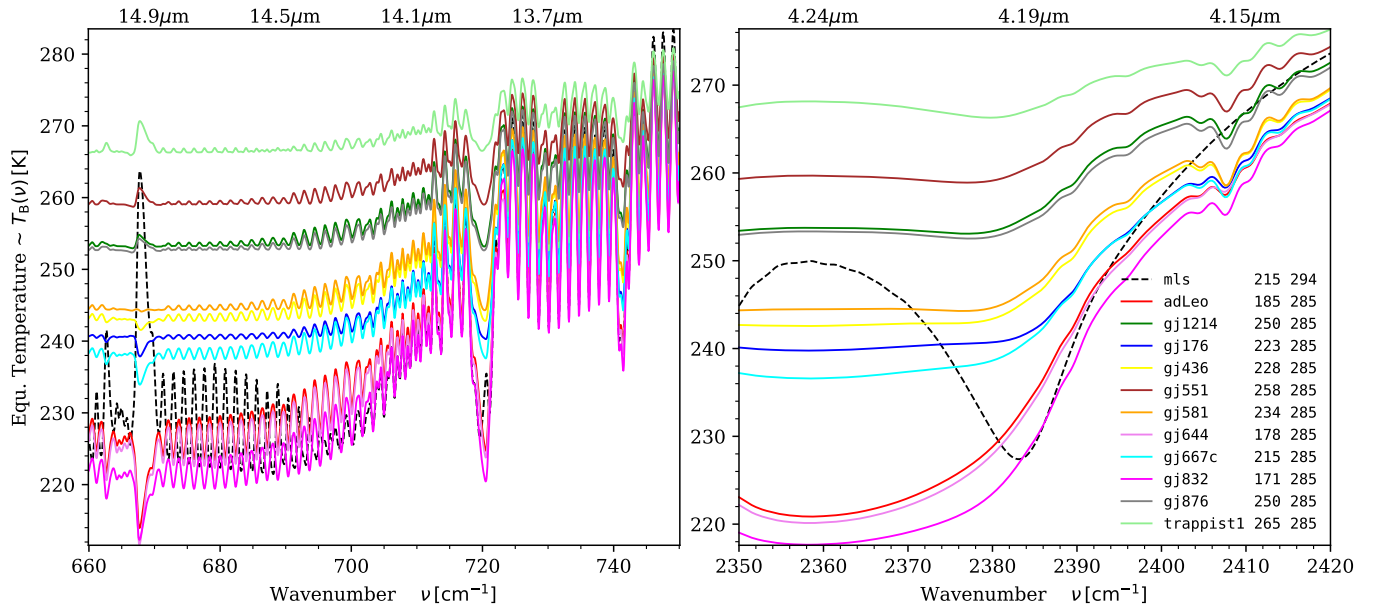


Figure 2. “Observed” equivalent brightness temperatures T_B (5) of hypothetical Earth-like planets orbiting the M-dwarfs indicated in the legend. Earth’s MLS atmosphere is shown for comparison (see subsection 2.4). Gaussian response function of HWHM $\Gamma = 0.25 \text{ cm}^{-1}$ (longwave, left) and $\Gamma = 1.0 \text{ cm}^{-1}$ (shortwave, right). For clarity no noise has been added. The TIR-LW and TIR-SW spectra comprise 1441 and 281 pixels, respectively. The numbers in the legend list the minimum and maximum atmospheric temperature [K]. Wavelengths are given at the top (numerically $\lambda[\mu\text{m}] = 10^4/\nu[\text{cm}^{-1}]$).

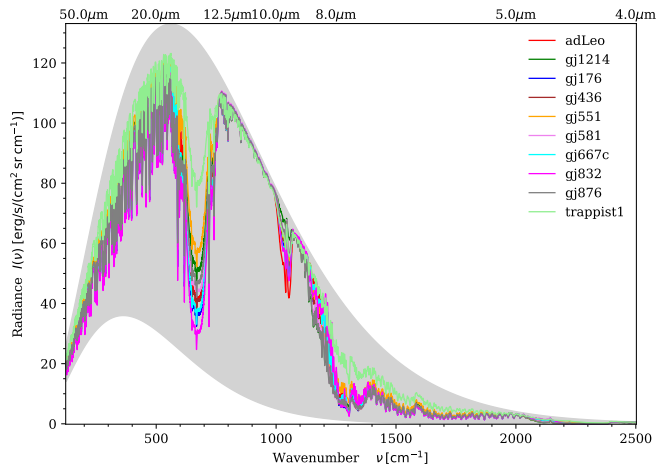


Figure 3. ToA intensities for M-Earths. The gray-shaded area indicates the Planck function $B(\nu, T)$ for the minimum and maximum atmospheric temperatures $T_{\min} \approx 171 \text{ K}$ for GJ 832 and $T_{\max} \approx 286 \text{ K}$ by “construction”. (Computed with GARLIC using atmospheric data from 1D-TERRA (Wunderlich et al. 2020); Gaussian response function with resolution $R = 1000$.)

generic Gaussian noise (generated by the Numeric Python `numpy.random.randn` function) independent of wavenumber,

The equivalent brightness temperature spectrum is obtained by “inversion” (5) of Planck’s function and depicted in Fig. 2 for noise-free simulated observations (see next subsection).

2.4 Data

Atmospheric data for Earth are taken from the “AFGL Atmospheric Constituent Profiles” atmospheres (Anderson et al. 1986) provid-

ing pressure and temperature vs. altitude along with concentration profiles for 28 gases including water vapor, carbon dioxide (with 360 ppm volume mixing ratio (VMR)), ozone, methane.

Atmospheric data for the assumed Earth-like planets around M-dwarfs (henceforth called “M-Earths”) are taken from Wunderlich et al. (2019). These temperatures and concentrations are inferred from a 1D photochemistry model (Gebauer et al. 2018) coupled to a climate model and are defined on 64 levels with a ToA pressure of about 0.08 mb. The former work assumed hypothetical planets with Earth’s properties orbiting different M-dwarf stars placed at the location where the planet receives modern Earth’s instellation. For all M-Earths the surface temperature is approximately 288 K by appropriate selection of the orbital radius, and the CO_2 VMR is about 355 ppm in the lower atmosphere.

Data for Trappist-1e from Wunderlich et al. (2020) are derived from the Berlin 1D steady-state, cloud-free, radiative-convective photochemical model 1D-TERRA. This dataset comprises dry&dead, wet&dead, and wet&live scenarios for CO_2 surface partial pressures of 10^{-3} , 10^{-2} , 10^{-1} , and 10^0 bar (corresponding to VMRs of approximately 10^{-3} , 10^{-2} , 10^{-1} , and $0.5 \cdot 10^0$ (see Table 11 in Wunderlich et al. (2020) and is indicated by the exponent in subsection 3.7). For comparison, the Trappist-1 planet of the M-Earth dataset (Wunderlich et al. 2019) has a VMR of 355 ppm in the lower atmosphere. Note that this planet is a purely hypothetical “Earth” orbiting Trappist-1, whereas the Trappist-1e scenarios are based on orbital and stellar data (see Section 3.2 and Table 9 in Wunderlich et al. 2020).

The Chahine approach delivers temperatures only at a small set of altitudes, but data on a moderately dense grid from BoA to ToA are required for the radiative transfer modeling and we will use function expansion for inter/extrapolation (see subsection 3.5). For the generation of the singular vectors to be used as base vectors for this expansion we use the set of 42 Earth atmospheric profiles collected by Garand et al. (2001) augmented with the eleven M-Earth temperatures regridded to a uniform altitude grid with 2 km

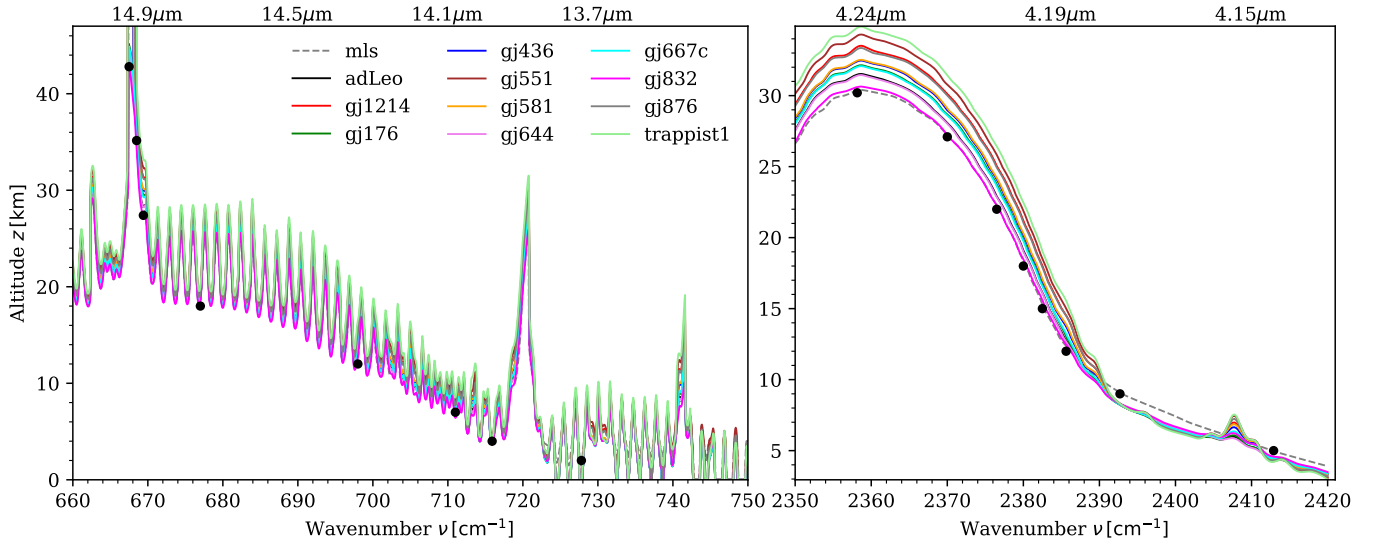


Figure 4. Weighting function maxima in the longwave TIR ($\text{CO}_2 \nu_2$ band at $15 \mu\text{m}$ with Gaussian response function of half width $\Gamma = 0.25 \text{ cm}^{-1}$, left) and shortwave TIR ($\text{CO}_2 \nu_3$ band at $4.3 \mu\text{m}$ with $\Gamma = 1.0 \text{ cm}^{-1}$, right). The length of these spectra (i.e. number of data points) is identical to those of Fig. 2. The black dots indicate manually selected $\nu \leftrightarrow z$ pairs (as also shown in Fig. 1 lower left).

steps (Schreier et al. 2020, subsection 3.2). Note that the first six Garand atmospheres correspond to the AFGL data.

Molecular line parameters are taken from the HITRAN database; instead of the most recent data (Gordon et al. 2022) (clearly mandatory for analysis of real observations) we use data from the initial 1986 release (Rothman et al. 1987) to speed-up the computations. (See the further discussion in subsection 4.3.) Only the main IR absorbers are considered, i.e. CO_2 and the interfering species H_2O , CH_4 , and O_3 .

See also Schreier et al. (2020) for more details on atmospheric and molecular data and a discussion of some of our approximations and assumptions.

3 RESULTS

3.1 First preliminary constraints

Inspection of the Schwarzschild equation (1) can be used for a first estimate of the range of atmospheric temperatures. Replacing the height-dependent temperature $T(z)$ in the Planck function by the minimum atmospheric value T_{\min} , the equation simplifies to $I(\nu) = B_{BoA}e^{-\tau} + \int B e^{-\tau'} d\tau' \geq B_{\min} (e^{-\tau} + (1 - e^{-\tau})) = B_{\min}$, hence the ToA radiance is greater (or equal) to the minimum Planck function. The upper limit can be derived in a similar manner, hence $B_{\min} \leq I(\nu) \leq B_{\max}$.

The intensities shown in Fig. 3 confirm these constraints, i.e. the lower and upper ‘‘Planck envelope’’ can be used as a preliminary estimate of the temperature range. The minimum and maximum atmospheric temperatures can then be readily estimated from the corresponding EBT minima and maxima.

The EBT spectra in Fig. 2 are, except for resolution, essentially a zoom-in on the intensity spectra of Fig. 3 transformed via Eq. (5). In addition to the strong absorption at $15 \mu\text{m}$ due to CO_2 the ozone fundamental band at 1042 cm^{-1} ($9.6 \mu\text{m}$) is clearly visible in Fig. 3.

3.2 Mapping Wavenumbers to Altitudes

Before estimating atmospheric temperatures from IR spectra according to the recipe of Eq. (5) several issues have to be addressed. First a set of appropriate wavenumber-altitude pairs has to be identified. Suitable wavenumbers are conveniently searched for in absorption band(s) of a molecule with well-known concentration and ideally little variability, e.g. the shortwave or longwave TIR bands of CO_2 . The corresponding altitudes are given by the location of the weighting function maxima, hence depend on the properties of the transmission \mathcal{T} and as a consequence depend on atmospheric temperature, pressure, and composition. Obviously these data are unknown for exoplanets, but fortunately weighting function of Earth-like exoplanets (with $\text{N}_2\text{-O}_2$ dominated atmospheres) are rather similar and closely resemble weighting functions of typical Earth climates, see Fig. 4. Accordingly we will use the $\nu \leftrightarrow z$ mapping of Earth’s atmosphere, e.g. for midlatitude and subarctic summer or winter (MLS, MLW, SAS, SAW) in the ν_2 longwave (LW, wavelength $\lambda \approx 15 \mu\text{m}$) and ν_3 shortwave (SW, $\lambda \approx 4.3 \mu\text{m}$) bands of CO_2 . Note that these spectra also depend on resolution (compare Figures 1 and 2 of Schreier et al. (2020)), hence a lower resolution leads to smoother spectra and reduces the sensitivity to upper atmospheric layers (See the discussion in subsection 4.1).

3.3 First Guesses — Selected Data in TIR-LW

Having identified the translation from wavenumber to altitude space (henceforth called ‘‘mapping’’) it appears to be straightforward to infer the temperatures from the observed spectrum using Eq. (5). However, both real spectra as well as our theoretical spectra simulating planned instrumental measurements (see Fig. 2) are contaminated by noise, and exploiting single data pairs ($\bar{\nu}, T_B$) is likely to lead to a ‘‘noisy’’ temperature profile. This is confirmed by Fig. 5 where the temperature retrieval for a hypothetical Earth-like planet orbiting AD Leo (Wunderlich et al. 2019) is illustrated: the inset shows the eight temperature values taken from the observed noise-free observation (intensity spectrum $I(\nu)$ converted to EBT $T_B(\nu)$ according

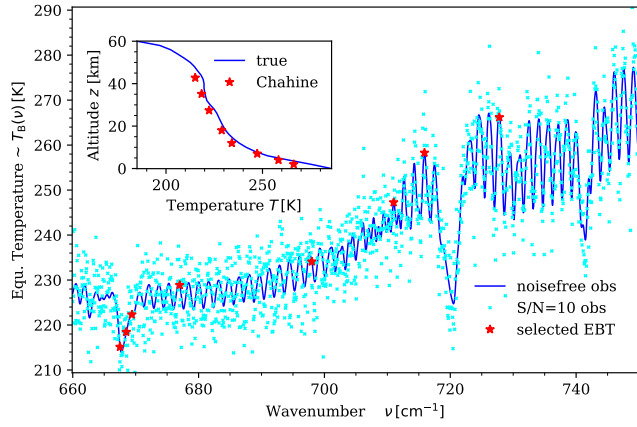


Figure 5. Estimate of AD Leo atmospheric temperature using a $\nu \leftrightarrow z$ mapping with 8 pairs for MLS (see Fig. 4). The main plot shows the ideal noise-free “observed” EBT (blue), the noise contaminated EBT spectrum ($S/N = 10$, cyan), and selected EBT values taken from the noise-free spectrum; the inset compares the estimated temperatures with the true profile. (TIR-LW 660–750 cm^{-1} ; Gaussian with $\Gamma = 0.25 \text{ cm}^{-1}$.)

to (5)). However, estimating these temperatures from the noisy EBT spectrum would clearly lead to a zigzag temperature profile.

To compensate for the noise the average of some neighboring pixels from the observed EBT spectrum can be used instead. Figure 6 depicts temperature estimates for the eleven M-Earth atmospheres (taken from Wunderlich et al. (2019) and already used in Schreier et al. (2020)) and clearly demonstrates that averaging EBTs from larger windows (e.g. 10 or 20 pixels) leads to the inferred temperature profile becoming smoother. Averaging 20 pixels leads to a significantly reduced zigzag, however, profiles estimated from two different measurements (model spectrum contaminated by two randomly generated noise vectors) are still distinct. For the M-Earths these first guess temperatures are encouraging, for some cases almost “perfect” (e.g. AD Leo, GJ 644, and GJ 832 even without averaging), but in a few other cases (e.g. GJ 551, GJ 876, and Trappist-1) deviations to the true profile are clearly visible. Moreover, temperatures of Trappist-1 in the lowermost altitudes are significantly underestimated.

The profiles of GJ 551, GJ 876, and Trappist-1 show oscillations of up to a few Kelvin. The cold trap of Trappist-1 is not very strong, i.e. the minimum temperature is only 20 K cooler than the maximum temperature (288 K at BoA). The tropopause temperatures of GJ 551 and GJ 876 are slightly cooler (258 K, and 251 K, respectively). Moreover, the local temperature maximum of Trappist-1 in the mid atmosphere at about 38 km is only modest and not reproduced by the EBT estimate. Overall however, the results are rather encouraging.

3.4 First Guesses — Exploiting the entire TIR-LW

Despite the promising results there are some caveats. Exploiting just a few data points implies that the majority of data remain unused. Moreover, the hand-picked selection of $\nu \leftrightarrow z$ mapping pairs is somewhat arbitrary, and the estimated atmospheric temperatures are therefore likely to change with different mappings. Consider for example the mapping pairs (677 cm^{-1} , 18 km), (698 cm^{-1} , 12 km), (711 cm^{-1} , 7 km) (cf. Fig. 4): One issue is whether the mapping wavenumber should be chosen to lie in the valley or on the peak of the absorption line.

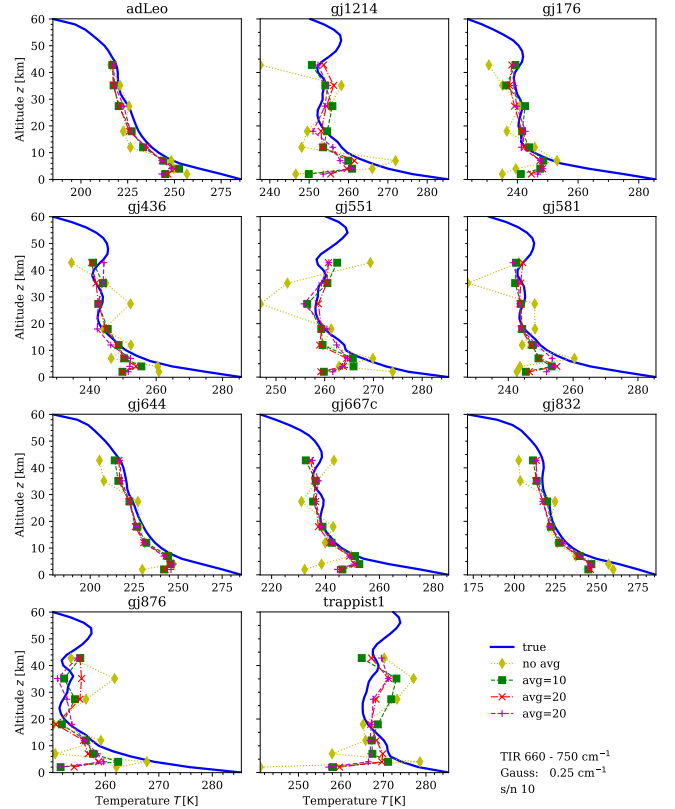


Figure 6. First estimate of M-Earths’ atmospheric temperatures using a $\nu \leftrightarrow z$ mapping with 8 pairs for MLS (see Fig. 4). The red and magenta curves labeled “avg=20” are identical except for the different noise vector. (Spectra as in Fig. 5)

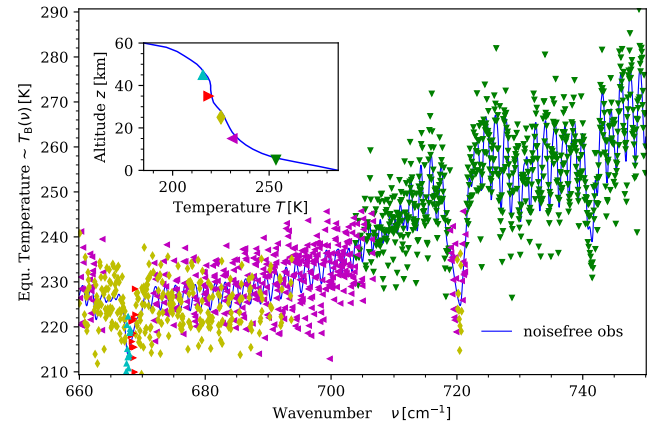


Figure 7. Estimate of AD Leo atmospheric temperatures using all $\nu \leftrightarrow z$ pairs for MLS. The colors and symbols for the $S/N = 10$ observation indicate the altitude range where radiation is mainly coming from according to the weighting functions. (For example green and cyan triangles for the lowest and highest altitude. Inset similar to Fig. 5, spectra as above.)

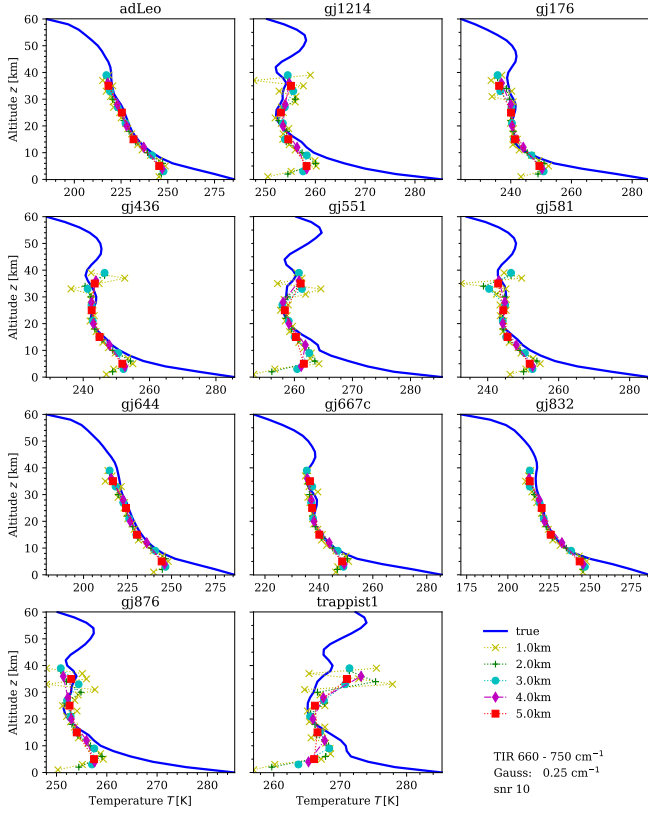


Figure 8. Estimate of M-Earths’ atmospheric temperatures using all MLS $\nu \leftrightarrow z$ pairs. For the 1.0 km and 5.0 km tolerance mappings 18 and 4 altitudes have been found with $5 \leq z \leq 39$ km and $5 \leq z \leq 35$ km, respectively. (Spectra as above.)

Choosing a point somewhere in-between is less sensitive to resolution and less likely sensitive to noise. Furthermore, the number of pixels which are used for averaging to account for the noise is limited, in order to avoid overlap of spectral regions. This is especially the case near the band center.

Figure 4 indicates that (except for the bottom and top altitudes) several wavenumbers are sensitive to a particular altitude. For example, the atmospheric layer around 32 km influences the radiance at several wavenumbers in the $660 - 670 \text{ cm}^{-1}$ interval and near 720 cm^{-1} (for some planets only). In order to address this issue, we therefore use the mean EBT of all pixels contributing to a particular altitude according to the weighting function peak height spectrum (Fig. 4). Because these peak altitudes rarely coincide exactly to a given grid point we accept all pixels within a given *tolerance interval* δz , i.e. to estimate the atmospheric temperature at an altitude z we take the average of all EBTs at wavenumbers with a weighting function peak height in the interval $[z - \delta z, z + \delta z]$. This concept is illustrated in Fig. 7 for a 5 km tolerance: Altitudes beyond 40 km are seen only in a narrow interval around 667 cm^{-1} , and the average of all EBT’s in this interval is interpreted as atmospheric temperature in the 40–50 km altitude range. Likewise, temperatures for altitudes below 10 km are estimated from EBT’s at wavenumbers beyond 700 cm^{-1} (except for the peak at 720 cm^{-1}).

Figure 8 compares results for all M-Earths and for various δz -intervals. In accordance with Fig. 4 no mappings are found for the upper atmosphere, and the highest altitude point estimated depends on the magnitude of the tolerance δz . In the “middle atmosphere” the

estimated temperatures are roughly equivalent. In some cases (e.g. GJ 664 or GJ 832) where temperatures were slightly underestimated using 8 (ν, z) pairs only, the deviation is reduced or eliminated. For the generalised Chahine case the retrieved temperatures are often smoother compared to Fig. 6. Moreover, the extended retrievals are less sensitive to noise: temperatures estimated with the 5 km tolerance from two observations with different noise vectors are largely identical except for the highest values (at 35 km) of GJ 551 and Trappist-1 (compare the two “avg=20” estimates in Fig. 6). The warm M-Earths (GJ 551, GJ 876, and Trappist-1) remain problematic with clear oscillations above about 30 km and considerably underestimate near BoA especially for the 1 and 2 km tolerances, but otherwise the retrieved and true temperature profiles are in good agreement with deviations to T_{true} less than ten Kelvin.

The oscillations of the profiles estimated with the 1 or 2 km tolerances can be interpreted as follows: A closer look to Fig. 1 shows that the bell-shaped weighting functions have a finite width of several kilometers in the lower atmosphere and almost 10 kilometers in mid to the upper atmosphere. Hence retrieving temperatures with one kilometer resolution is questionable.

3.5 Iterative Refinements — TIR-LW

The temperature estimates presented in the previous subsection are not always satisfactory, but they can be used as initial guesses for the Chahine relaxation scheme (6) or other iterative solvers like nonlinear least squares (e.g. Schreier et al. 2020). Clearly the main advantage is the computational speed, i.e. the whole “retrieval” is simply the inversion (5) of the Planck function and therefore can be performed within fractions of a second. However, because the peak heights of the weighting functions do not cover the entire altitude range, this initial guess temperature values cannot readily be used as an input for radiative transfer modeling. Moreover, with the 4 or 5 km tolerances only few temperature values are estimated in the mid atmosphere.

Extrapolation appears to be a tempting solution, but this is well known to be problematic. In Schreier et al. (2020) (Fig. 5) we have shown that Earth-like temperature profiles can be represented as a linear combination of some base vectors resulting from a singular value decomposition (SVD) of a large matrix comprising “representative” temperatures (comprising the 42 Garand atmospheres and the 11 M-Earth atmospheres introduced in subsection 2.4). Hence we will use here a linear least squares fit to determine the expansion coefficients for the “Chahine initial guess” profile and then “extrapolate” this profile to the entire altitude range. In addition this is used for interpolation to a dense altitude grid in the lower and mid atmosphere appropriate for radiative transfer modeling. (For brevity this will be called “extrapolation” henceforth.)

Before starting the iterations according to (6) one more issue has to be discussed: how to stop the process. For nonlinear least squares solvers such as MINPACK (More 1978) or NL2SOL (Dennis, Jr. et al. 1981a,b) two convergence criteria are usually employed: firstly the change of the estimated state vector (here temperature) is small and the change of the residual norm (the norm of the model minus observed signal vector, here the radiance spectrum) is small (where “small” should be related to S/N). Inspection of the radiance residual norm is clearly a natural choice for least squares. Exploiting the deviation of the fitted temperature to the true temperature or the deviation of the model to the “true” spectrum is clearly impossible for analysis of true observations and is hence not used as a convergence criterion.

For the analysis of the TIR-LW spectra using iterative Chahine relaxation (6) we start with, e.g., Earth’s SAW atmospheric data; the

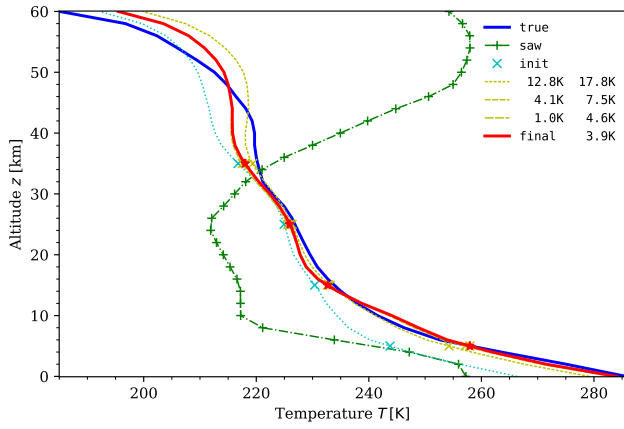


Figure 9. Chahine relaxation for AD Leo starting with SAW pressure, temperature (green), and concentrations ($S/N = 100$, TIR-LW). The cyan crosses show the initial guess (5) (similar to Fig. 7) and the cyan dotted line its extrapolation. Intermediate temperature profiles (6) are shown in yellow, the numbers in the legend indicate the maximum temperature change ($T_{i+1} - T_i$) and maximum EBT deviation (observed - model). The red curve shows the final temperature profile with the maximum EBT deviation in the legend.

SAW temperature is needed to compute the atmospheric transmission \mathcal{T} and surface emission I_{surf} in Eq. (5). The following stopping criteria have been used: a maximum change of the updated temperature less than 5 K or a maximum change of the EBT of less than 5 K. For all M-Earths the relaxation stops after two or three iterations (see Fig. 9 for an illustrative example). The results (Fig. 10) are consistent with those of Fig. 8: for most planets the temperature is retrieved quite well for altitudes below about 40 km, but GJ 551 and Trappist-1 (and to a lesser extent GJ 1214) appear to be problematic. Nevertheless, for all planets the cold trap temperatures closely resemble the true one, and even for Trappist-1 the absolute temperature differences are small.

Further runs with other Earth model data (MLS, MLW, SAS, and tropical) essentially confirm these findings, see Fig. 10. For planets with very low minimum temperatures (AD Leo, GJ 644, or GJ 832) all models lead to almost identical temperatures with small differences only in the upper atmosphere. Differences are clearly visible for GJ 1214, GJ 551, GJ 876, and Trappist-1, i.e. planets with relatively high minimum temperatures.

Although the most favorable model is unknown for real observations we can nevertheless use the minimum radiance residuum norm $\|\Delta J\| = \|I_{\text{obs}} - I_{\text{mod}}\|$ as a hint for selection of the “best” fit. In all but two cases this selected solution corresponds to the optimum solution according to the minimum norm of the EBT difference spectrum ΔT_B : for GJ 551 and GJ 876 MLS give the smallest EBT difference, whereas SAS and TRO yield the smallest radiance difference (however, both norms are identical within four digits). Using the mean EBT difference as criterion gives also different solutions for GJ 581.

In addition to the retrievals using the five Earth models Fig. 10 also shows the temperature fitted with the correct exoplanet pressure and composition (clearly unknown in case of real observations); the initial guess temperature required to compute the weighting functions and total atmospheric transmission $\mathcal{T}(\nu, 0)$ is set to the mean EBT. Interestingly the norm of the radiance difference with the correct exoplanet composition is smaller than the norm with the best Earth composition only for some of the planets. However, Table 1 indicates that the variability of these residual norms is always small, the difference of the largest and smallest norm is less than a few percent, and

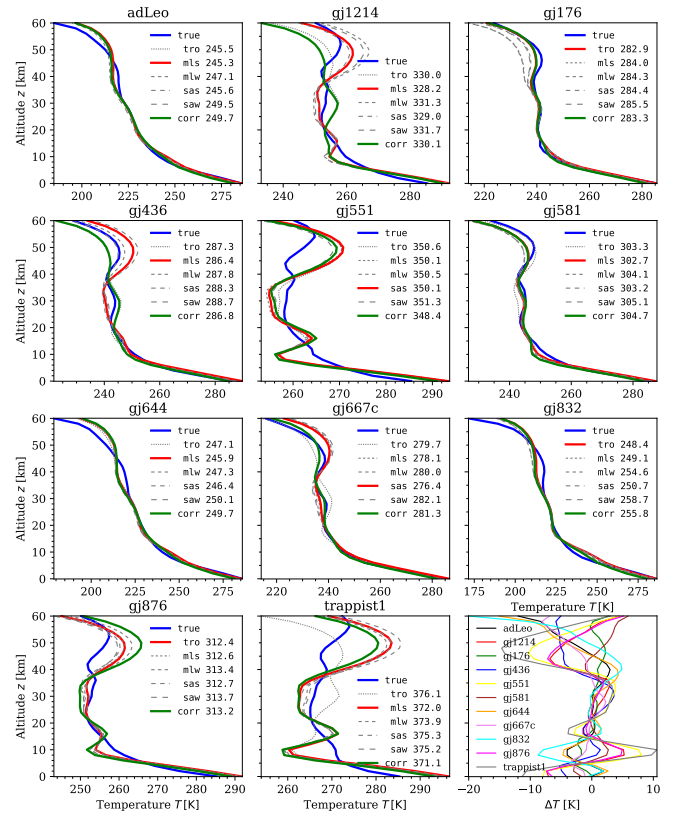


Figure 10. Comparison of atmospheric temperatures using Chahine relaxation for all Earth data (specified in the legend). The red solid line indicates the best fit according to the norm $\|\Delta J\|$ of the residual radiance spectrum (in units $\text{erg/s}/(\text{cm}^2 \text{sr cm}^{-1})$, see legend). The green temperature shows the fit using the correct atmospheric densities. The last subplot shows the temperature differences (true - fit) for the best Earth model. (All $\nu \leftrightarrow z$ pairs with 5 km tolerance, extrapolation with 4 base vectors, TIR-LW spectra as above.)

Table 1. Comparison of the radiance residuum norms (in radiance units $\text{erg/s}/(\text{cm}^2 \text{sr cm}^{-1})$) for iterative Chahine relaxation with the correct atmospheric pressure and concentrations with fits using one of Earth’s model atmospheres. The “min” and “max” columns give the range of residuum norms for these fits. The second column lists the range of atmospheric temperatures, i.e. $\max(T) - \min(T)$ in Kelvin.

	ΔT	$S/N = 10$		$S/N = 100$			
		corr.	min	max	corr.	min	max
AD Leo	100.6	249.7	245.3	249.5	42.43	41.2	49.2
GJ1214	35.1	330.1	328.2	331.7	58.94	60.4	71.5
GJ176	62.0	283.3	282.9	285.5	40.73	43.8	51.6
GJ436	56.7	286.8	286.4	288.7	32.14	36.6	47.4
GJ551	27.3	348.4	350.1	351.3	71.32	72.8	83.1
GJ581	51.5	304.7	302.7	305.1	34.03	39.0	48.7
GJ644	106.9	249.7	245.9	250.1	47.77	45.0	54.7
GJ667c	69.8	281.3	276.4	282.1	36.33	34.8	48.5
GJ832	114.2	255.8	248.4	258.7	60.31	47.8	67.6
GJ876	35.2	313.2	312.4	313.7	55.08	57.8	67.7
Trappist1	20.2	371.1	372.0	376.1	90.76	92.8	101.8

the residual of all fits is very large because of the significant noise of the synthetic intensities (i.e. the residual is dominated by noise).

For synthetic measurements with less noise the residual norm of fits with different atmospheric models shows larger variations up to 41% for $S/N = 100$ (because of the smaller noise the stopping criterium has been tightened to 3 K temperature change). Note that the variation of the norms is especially large for planets with a large range of atmospheric temperatures. Again the correct atmosphere does not always deliver the best fit, but the best Earth model and the correct densities always give similar temperature profiles. Table 1 shows that the correct densities do not yield a model spectrum closer to the observed spectrum for the four M-Earths with the largest temperature gradients ΔT (AD Leo, GJ 644, GJ 667c, and GJ 832).

At first glance this “failure” appears to be quite disturbing and we interpret this as follows: The residual norm is clearly the essential number characterising least squares, i.e. the quantity to be minimised. However, it is not the decisive quantity for Chahine relaxation; obviously the ratio of observed to model spectra in (6) should finally be close to one, but there is no uniquely defined number for the progress of the relaxation and quality of the solution.

These results may also be considered as a hint that Chahine relaxation relies on a strong simplification, i.e. the intensity (1) at a particular wavenumber can be approximated by the Planck emission at a particular altitude according to (4). This assumption clearly ignores the shape of the weighting functions (compare Fig. 1 bottom-left) and is apparently problematic when the temperature differences are large. Furthermore, large temperature differences make the extrapolation more difficult. Nevertheless, the last subplot of Fig. 10 demonstrates that in the mid atmosphere (about 15 to 35 km) the temperature can be estimated within ± 5 K.

3.6 TIR-SW

The shortwave TIR appears to be less favourable for temperature retrieval for several reasons: The radiance values in the TIR-LW are higher compared to the TIR-SW (Fig. 11 in Schreier et al. (2020)), the TIR-LW is more favourable because of the higher star-planet contrast, and the TIR-LW is also less affected by scattering. Moreover, the TIR-SW weighting function peak heights do not cover altitudes above 30 km (Fig. 4), and for shorter wavelengths reflection of thermal radiation at the surface is becoming increasingly important. On the other hand, the TIR-SW weighting functions indicate some more sensitivity to the lowest atmosphere, and in fact IR instruments of meteorological satellites used for sounding of Earth’s temperature (Menzel et al. 2018), e.g. AIRS (Chahine et al. 2006) and IASI (Hilton et al. 2012), exploit both regions.

Figure 11 depicts the temperature inferred from the equivalent brightness temperatures (5) in the TIR-SW using all $\nu \leftrightarrow z$ pairs for MLS. Considering altitudes within one or two kilometers around a weighting function peak height gives zigzag temperature profiles as in the longwave analysis, cf. Fig. 8. For the 5 km tolerance the profiles are smoother, however only four temperature values for the upper troposphere and lower stratosphere are estimated. Compared to the TIR-LW estimates, Fig. 8, the profiles appear to be somewhat smoother and closer to the true temperature. Trappist-1, however, is reasonable only in the 10–20 km range. For other Earth mappings (MLW, SAS, SAW, tropical) temperatures are almost identical (not shown).

In Fig. 12 results from temperature estimates using the SW and LW interval individually are compared with those from the combined spectrum (with 1722 data points, cf. Fig. 2). The “data fusion” product clearly benefits from the sensitivity of the longwave spectrum beyond

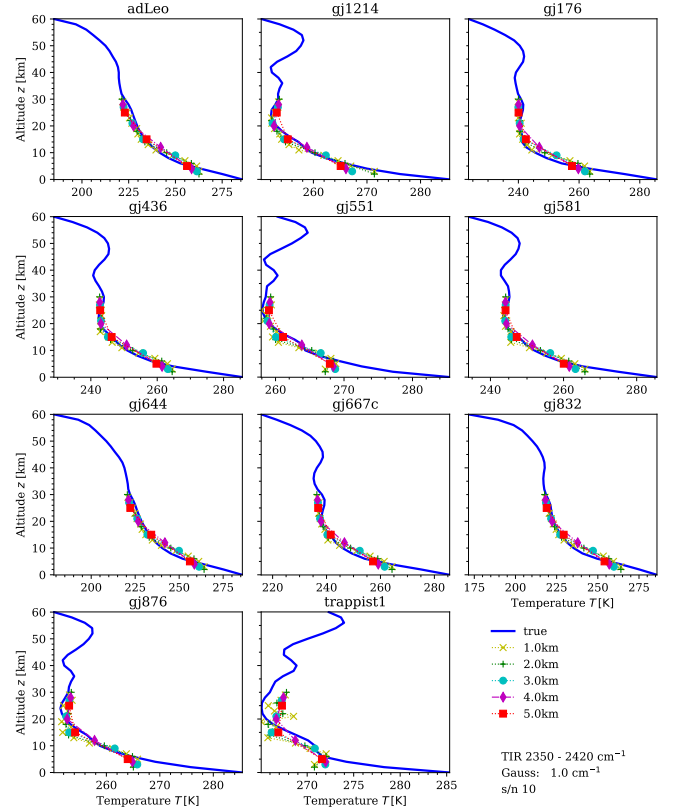


Figure 11. Estimate of atmospheric temperatures using all $\nu \leftrightarrow z$ pairs for MLS and TIR-SW ($2350 - 2420 \text{ cm}^{-1}$, $S/N = 10$, Gaussian with $\Gamma = 1.0 \text{ cm}^{-1}$.)

30 km; however, it also inherits the underestimated temperature in the lowest atmospheric levels, especially for GJ 1214, GJ 551, GJ 876, and Trappist-1. A more sophisticated data fusion approach might possibly be able to avoid the shortcomings of the TIR-SW in the upper atmosphere and TIR-LW in the lower atmosphere.

3.7 Trappist-1e

The Trappist-1 planetary system (Gillon et al. 2017) orbiting a nearby M-dwarf has attracted considerable attention because several terrestrial-type exoplanets lie in the circumstellar habitable zone (e.g. Barstow & Irwin 2016; Grimm et al. 2018; Krissansen-Totton et al. 2018; Lustig-Yaeger et al. 2019; Fauchez et al. 2020; Krissansen-Totton & Fortney 2022). Planets e and f have been the object of numerous studies (e.g. Barstow & Irwin 2016; Morley et al. 2017b; Mikal-Evans 2021). Recently, Wunderlich et al. (2020) have used the newly developed radiation–convection–photochemistry model 1D-TERRA to study the feasibility of atmospheric characterisation, in particular the possibility of finding any evidence for an ocean or biosphere.

Here we use these dry&dead, wet&dead, and wet&live scenarios with varying CO_2 levels (see subsection 2.4) for further tests of the Chahine methodology. We generate synthetic observations in the same way as for the M-Earths (Fig. 2), i.e. monochromatic intensity spectra according to (1) are convolved with a Gaussian and contaminated with noise.

Figure 13 is similar to Fig. 12 and shows atmospheric temperatures retrieved from the TIR-LW and TIR-SW equivalent brightness

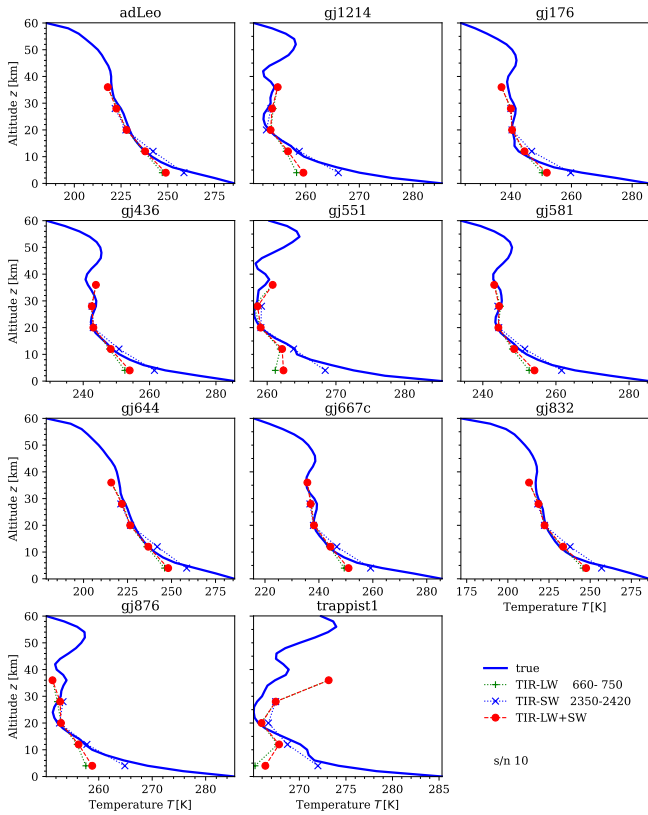


Figure 12. Comparison of atmospheric temperatures estimated from the TIR-SW, the TIR-LW, and the concatenated spectrum. (All $\nu \leftrightarrow z$ pairs with a 4 km tolerance for MLS, $S/N = 10$)

temperatures (5) using the MLS weighting function peak altitudes (cf. Fig. 4) with a 4 km tolerance (without iteration). The LW and SW estimates are quite similar and relatively smooth. For the CO_2 VMR = 10^{-3} atmospheres (bottom row) the temperature near BoA is somewhat underestimated, but in the middle atmosphere up to about 40 km the estimates are close to the truth. However, for the atmospheres with larger CO_2 concentrations the temperatures are clearly too cool.

Due to the large mixing ratios the atmospheres are optically thick in the spectral windows considered here, and radiation (photons) from the lower warm altitudes cannot propagate upwards to ToA (and the observer). This interpretation is confirmed by the range of equivalent brightness temperatures given in the plot, i.e. the warm low atmosphere does not show up in the EBT spectra. Analysis of effective height spectra (Fig. 14) that might be available from primary transit spectroscopy also indicates that the TIR-LW interval ($660 - 750 \text{ cm}^{-1}$) is insensitive to the lower atmosphere.

Furthermore, the success of the temperature estimates for the VMR = 10^{-3} cases suggests that the $\nu \leftrightarrow z$ mappings of Earth’s atmospheres are not adequate for Trappist-1e atmospheres with more carbon dioxide. Fig. 15 shows that with higher CO_2 concentrations the location of the weighting function maxima move upwards by 5 or even 10 km, whereas the “nature” of the planet (wet vs. dry, dead vs. alive) does not have a big impact.

In summary, Figures 14 and 15 suggest that atmospheres with abundant CO_2 are not well reproduced from TIR-LW and TIR-SW spectra especially in the lower regions (Fig. 13). Therefore we also considered an extended spectral range along with the correct weight-

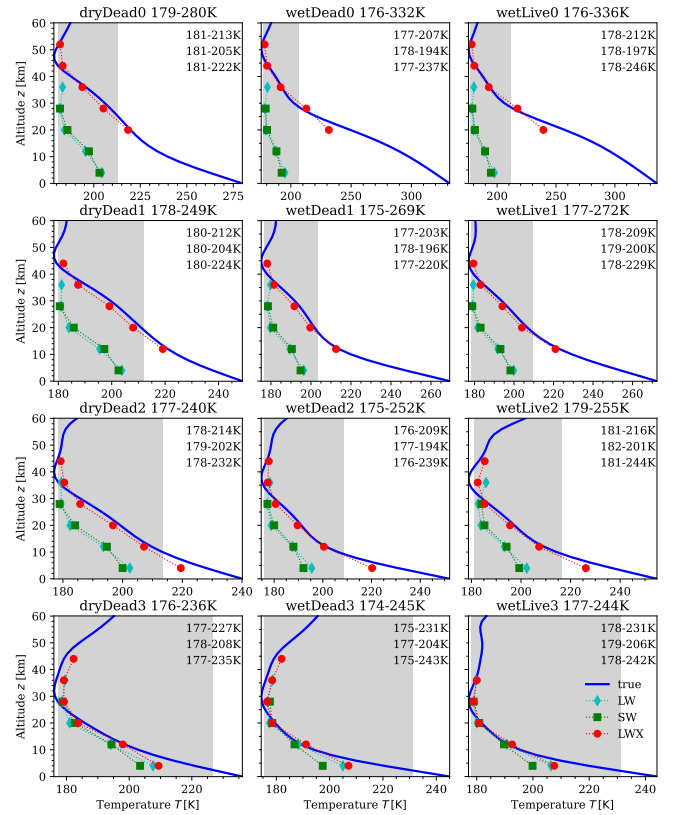


Figure 13. Trappist-1e temperatures from TIR-LW ($660 - 750 \text{ cm}^{-1}$ with $\Gamma = 0.25 \text{ cm}^{-1}$, cyan diamonds) and TIR-SW ($2350 - 2420 \text{ cm}^{-1}$ with $\Gamma = 1.0 \text{ cm}^{-1}$, green squares) with entire $\nu \leftrightarrow z$ MLS map. Third estimate with an extended TIR-LW (LWX, $660 - 850 \text{ cm}^{-1}$, red circles) and the correct map (i.e. correct CO_2). (All spectra with $S/N = 10$). The number n immediately following the planetary scenario description in each subplot title indicates the CO_2 surface partial pressure, i.e. $p_{\text{CO}_2} \approx 10^{-n}$ bar. (Regarding notation see subsection 2.4.) Minimum and maximum atmospheric temperatures are listed in the title, the range of the EBTs of the noise-free LW, SW, and LWX spectra are given inside the plot. The gray shaded area shows the EBT range for the SW and LW combination.

ing function peak heights (i.e. weighting functions in the extended TIR-LW computed with the true concentrations) which considerably improved the estimate (esp. in the mid atmosphere, Fig. 13 red dots; however, the sensitivity to the lower atmosphere is lost, i.e. no mappings with altitudes below 10 or 20 km for the 10% and 50% CO_2 planets).

Having demonstrated that atmospheric temperatures can be estimated from equivalent brightness temperatures (5) using an extended TIR-LW interval if the composition is known, we now examine iterative Chahine relaxation (6). The assumption of known abundances appears reasonable since some objects will have information from transmission spectra. In particular quantifying CO_2 might be possible due to e.g. its dominant absorption bands (clearly visible around 660 cm^{-1} and 2400 cm^{-1} in Fig. 14); concentration estimates for other gases however might be more difficult.

First we examine whether we can then distinguish the temperature profiles for the three scenarios (wet vs. dry, dead vs. live), i.e. we compare retrievals using different surface and lower atmosphere scenarios (for example, for the wet&live planet “observation” (right column in Fig. 16) we also investigate fits using boundary parameters of the dead scenarios with the correct CO_2).

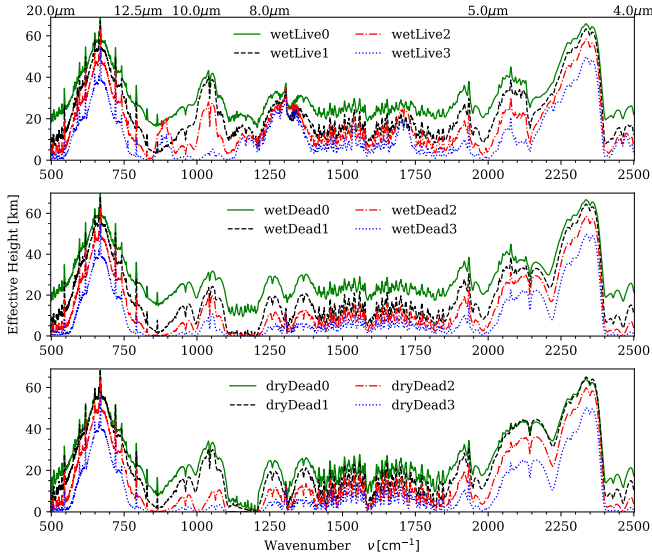


Figure 14. Trappist-1e effective heights for a Gaussian response function with $R = 1000$. (Computed with GARLIC.)

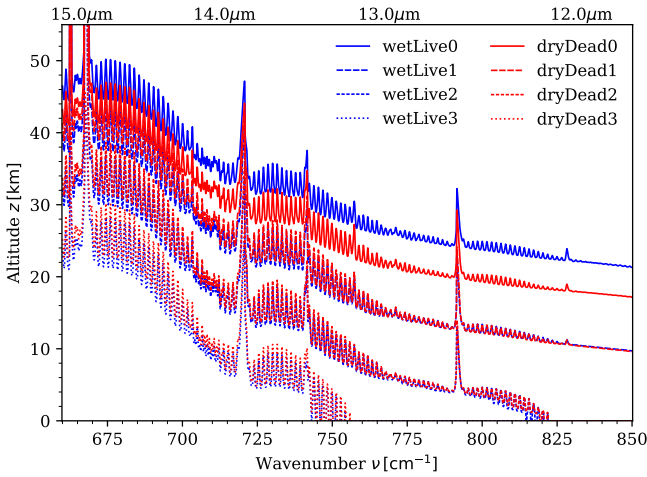


Figure 15. Trappist-1e altitudes of weighting function maxima in the extended LW-TIR (Gauss $\Gamma = 0.25 \text{ cm}^{-1}$). The wet&dead weighting function maxima are largely similar to the wet&live maxima.

Figure 16 (top) shows that the effect of changing the scenario is largest for the high CO_2 abundance: in the lower atmosphere temperature is significantly underestimated for the two dead scenarios which is likely related to the fact that the effective heights (Fig. 14) and weighting functions (Fig. 15) do not show any sensitivity to the lowest atmosphere (esp. for the wet cases). For the observation of the wet&live $\text{VMR} = 0.5$ planet (top right) both wet models yield an only moderately underestimated temperature. The difficulty of the high CO_2 atmospheres is also demonstrated by the increased number of iterations required for convergence. Fits with large residuum norm show the largest deviations between true and retrieved temperature in the mid atmosphere. For moderate and low CO_2 (other rows in Fig. 16) the impact of the scenarios is only weak, and only one or two iterations are necessary. Results here are close to the true profile (blue line) in the low and mid atmosphere, although deviations are

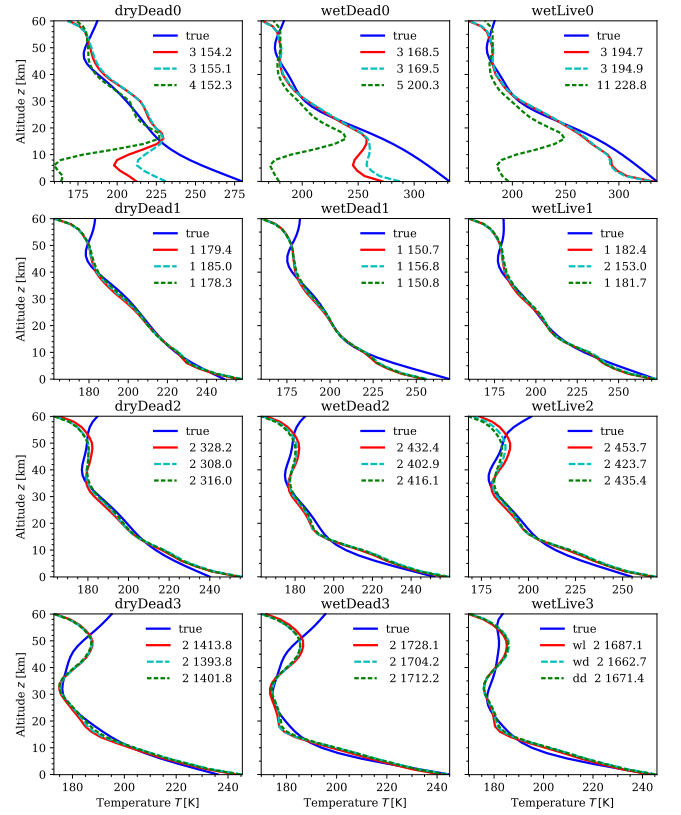


Figure 16. Chahine iterative estimate of Trappist-1e temperatures with correct CO_2 abundance and varying scenarios: wet & live (red), wet & dead (cyan long dashed), and dry & dead (green dashed). SVD “extrapolation” with four base vectors. Extended TIR-LW spectra as above. The legend lists the number of iterations and the radiance residual norm.

clearly evident in the upper atmosphere where the weighting function exhibits little sensitivity.

A second set of runs has been conducted assuming MLS molecular profiles scaled to the correct Trappist-1e column density, see Fig. 17. Similar to Earth the Trappist-1e atmospheres have CO_2 VMR profiles almost constant in altitude, and the H_2O VMRs are strongly decreasing for pressures below 100 mb (see Fig. 7 in Wunderlich et al. 2020). (In contrast the CO_2 VMR of all M-Earths increases by 10–20% for $p < 100$ mb (see Fig. 4 in Wunderlich et al. 2019).) However, at least for Earth, the total optical depth is essentially dominated by the CO_2 contribution (see Fig. A3 in Schreier et al. 2020), which suggests that for these Trappist-1e atmospheres with even higher CO_2 concentrations this dominance will be even stronger. Hence, the assumption of isoprofiles does not have a strong impact on the quality of the retrievals, i.e. temperature in the mid atmosphere can be estimated with little deviation from the truth.

Figure 17 also shows the importance of the “extrapolation” scheme based on the expansion using singular vectors. Although a temperature profile representation using only two base vectors delivers temperatures close to the true even for the lowest atmosphere (including the $\text{VMR} = 0.5 \cdot 10^0$ cases, top row), a profile expansion with three or four base vectors appears to be more reasonable. Using five base vectors works well for $\text{VMR} \leq 10^{-2}$, but clearly fails for very high CO_2 concentrations. The radiance residual norms shown in the plot also indicate that three or four base vectors can be used reliably except for the high CO_2 concentrations.

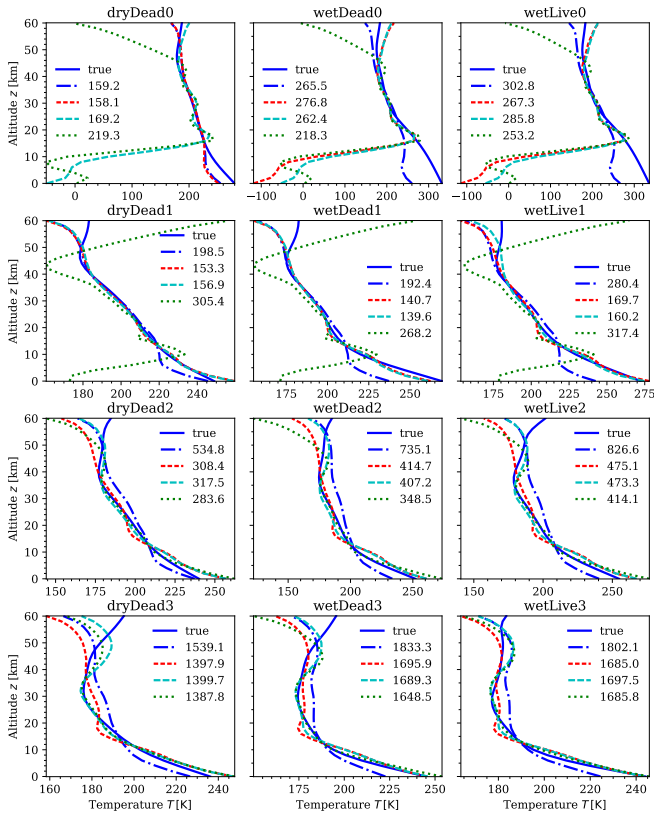


Figure 17. Chahine iterative estimate of Trappist-1e temperatures starting with MLS $v \leftrightarrow z$ mapping and molecular profiles with correct column density. The retrieved temperatures correspond to SVD “extrapolation” with two (blue dash-dotted), three (red dashed), four (cyan long dashed), and five (green dotted) base vectors. (Numbers in legend list the radiance residual norm, spectra as above.)

Further tests have also been conducted with reduced or increased CO_2 concentrations. For moderate changes with quarter, half, double and quadruple isoprofiles the retrieved temperature profiles are still close to the true temperature. (See the further discussion in subsection 4.7.)

4 DISCUSSION

4.1 Spectral resolution

The retrievals reported so far have been conducted assuming moderate resolution TIR-LW and TIR-SW spectra. The motivation for $R > 2500$ has been discussed in Schreier et al. (2020, Figure 1) where we showed that for decreasing resolution the sensitivity to upper atmospheric layers decreases: for a Gaussian response function with HWHM $\Gamma = 0.25 \text{ cm}^{-1}$ (corresponding to a resolution $R = 2800$ at 700 cm^{-1} (wavelength $14.3 \mu\text{m}$)) the maximum of the weighting function peak height spectrum (cf. Fig. 4) reaches altitudes above 40 km; a coarser resolution reduces the peak height (for $\Gamma = 1.0 \text{ cm}^{-1}$ ($R = 700$), $\Gamma = 2.0 \text{ cm}^{-1}$ ($R = 350$), and $\Gamma = 7.0 \text{ cm}^{-1}$ ($R = 100$)) the maxima lie at 40 km, 24 km, and 18 km, respectively).

The TIR-LW and TIR-SW CO_2 bands can be observed by the Medium Resolution Spectrometer (MRS) of the JWST Mid Infrared Instrument (MIRI) with a resolving power R of about 2500 (Rieke et al. 2015) (the Low Resolution Spectrometer (LRS) only sees the

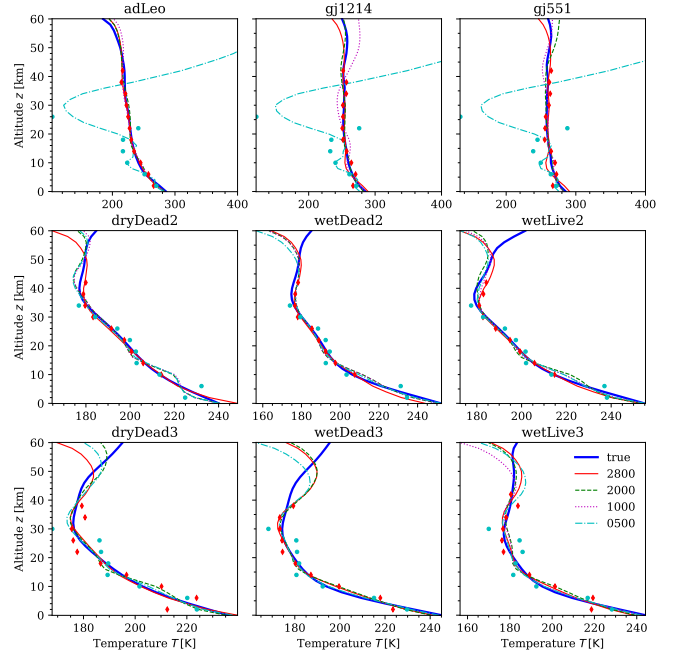


Figure 18. Impact of resolution on Chahine iterative temperatures estimates. MLS initial guess atmosphere, SVD “extrapolation” with 4 base vectors. The red diamonds and cyan circles show the final update according to the relaxation equation (6) for $R = 2800$ and $R = 500$, respectively. TIR-LW (M-Earths) or TIR-LWX (Trappist-1e). The solid, dashed etc. lines show the corresponding extrapolated temperature profiles.

TIR-SW band with a resolution $R = 100$). However, Morley et al. (2017b) caution that “for temperate planets spectroscopy with JWST-MIRI will likely be unrealistically expensive”. In the JWST Guaranteed Time Observations (GTO) program several exoplanets have already been observed with the Near Infrared Imager and Slitless Spectrograph (NIRISS), NIR Spectrograph (NIRSPEC), and NIR Camera (NIRCam) instruments, that can deliver spectra with wavelengths up to $5 \mu\text{m}$ at low and medium resolution.

For an assessment of the impact of resolution on the retrieval, synthetic observations have been generated with different resolutions for selected exoplanets. Noise has been adjusted assuming a square root relationship between resolution and S/N . The results depicted in Fig. 18 confirm the expectations discussed above, i.e. with decreasing resolution information on the upper atmosphere is diminishing. In particular, for $R = 500$ Chahine estimates according to (6) are only available for altitudes below 20 km (shown as cyan circles) and “extrapolation” is clearly problematic.

4.2 Surface emission

Apart from the type of inversion (least squares vs. Chahine relaxation) the methodology used here is largely identical to that of our previous feasibility study. However, there is one large difference worth discussing: in Schreier et al. (2020) we have ignored surface emission. Obviously the first term in (1) is mandatory for modeling IR spectra in atmospheric window regions where the atmosphere is relatively transparent such as the $800 - 1200 \text{ cm}^{-1}$ interval for Earth (except for O_3 absorption around $9.6 \mu\text{m}$). For the terrestrial exoplanets, transmission $\mathcal{T} \approx 0$ in the CO_2 bands considered in Schreier et al. (2020) (LW: $660 - 720 \text{ cm}^{-1}$), hence the surface contribution has no impact on mid atmospheric temperature estimates.

However, for wavenumbers beyond 720 cm^{-1} corrections cannot be neglected, so an estimate of the surface temperature is required. If wavenumbers with transmission close to one are observed, the corresponding radiance can be used to estimate T_{surf} . Here we approximate surface temperature by the largest equivalent brightness temperature observed, assuming that the maximum atmospheric temperature corresponds to the BoA temperature and is approximately equal to the surface temperature. (Although warmer temperatures are possible at the stratopause, these do not contribute strongly to the spectrum as indicated by the weighting functions (cf. Fig. 1)).

Due however to noise, the largest EBT may not always be the best estimate of the surface temperature. Alternatively the maximum of a smoothed EBT spectrum (e.g. by running averages) or the mean of the largest ten etc. values could be used.

4.3 Molecular spectroscopy data

Similar to Schreier et al. (2020) we have used the very first edition of the HITRAN database (Rothman et al. 1987) rather than the latest version to speed up the computations. This simplification appears to be justified for the feasibility study presented here, but is clearly inadequate for analysis of real observations. In our previous study we discussed the then latest 2016 version (Gordon et al. 2017), here we provide a brief update for the current HITRAN 2020 (Gordon et al. 2022).

For a realistic modeling of IR emission spectra in the $660\text{--}750\text{ cm}^{-1}$ interval line data in an enlarged interval have to be considered to properly account for line wing contributions and convolution with the spectral response function. Hence lines in the range $648.75\text{--}761.25\text{ cm}^{-1}$ are read: HITRAN 2020 knows 449445 lines of 29 molecules, which reduces to 79394 lines of the five main IR absorbers (CO_2 , O_3 , N_2O , CH_4 , H_2O). In contrast, HITRAN 86 returns 16003 lines of 4 molecules; furthermore removing weak lines results in 4255 lines total including 2827 lines of carbon dioxide. Despite this drastic reduction of active lines the final spectra do not change significantly: For the MLS atmosphere the peak height of the weighting function is modified by a few hundred meters only (except for $\Delta z \approx 0.8\text{ km}$ at the high wavenumber end of the interval); Likewise, the difference of the equivalent brightness temperature spectra is usually less than 1 K (with a maximum $|\Delta T_{\text{B}}| \approx 1.8\text{ K}$ at 718 cm^{-1}).

Air-broadened half-widths are listed in the HITRAN database since its beginnings half a century ago, whereas self-broadening was introduced later with the 1986 release (Rothman et al. 1987). Collision (pressure) broadening parameters for perturbers other than “air” (i.e. Earth’s N_2 , O_2) can be important for modeling spectra of other planets and were included only recently in HITRAN (Gordon et al. 2017). For the terrestrial $\text{N}_2\text{--O}_2$ dominated atmospheres considered here the HITRAN 86 broadening parameters are clearly appropriate (with the possible exception of the 50% CO_2 Trappist-1e scenarios). In this context it might also be worth noting that the line strengths in HITRAN are also tuned to Earth, i.e. the strengths are scaled by the relative natural abundance of the isotopes in Earth’s atmosphere.³

In addition to line transitions continua can be also important, especially water self and foreign continua (Shine et al. 2012) and collision induced absorption (CIA, Richard et al. 2012; Karman et al. 2019). Comparison of EBT spectra (MLS atmosphere, $R = 100$) computed with and without H_2O , CO_2 , O_2 and N_2 corrections (Clough et al. 1989) indicates negligible differences in the TIR-LW

regions considered here; however, in the TIR-SW differences up to almost 8 K show up around 2400 cm^{-1} in the right wing (short wavelength) of the CO_2 band. (For the entire TIR ($500\text{--}2500\text{ cm}^{-1}$) maximum differences up to $\approx 10\text{ K}$ at 1600 cm^{-1} can be seen.)

4.4 ToA 60 vs 120 km

In Schreier et al. (2020) all runs have been performed with a ToA at 60 km, mainly because the Garand et al. (2001) atmospheres are defined only for pressures down to 0.08 mb (about 60 to 65 km), but also to speed up the computations. Likewise, the M-Earth atmospheres of Wunderlich et al. (2019) have ToA altitudes in the range 61 to 74 km. However, for IR radiative transfer modeling altitudes up to about 100 km might be important (the AFGL data (Anderson et al. 1986) are given up to 120 km). For an assessment of the importance of the upper atmosphere we have compared radiances for 60 and 120 km ToA and the MLS atmosphere. In the TIR-LW region the EBT difference is usually less than 1 K except for the strong radiance peak at 668 cm^{-1} and in the right wings of the $\text{CO}_2\ \nu_2$ band.

4.5 Geometry

Observations of exoplanet thermal emission will deliver disk averaged spectra only, whereas we have used a single line-of-sight assuming a strict nadir view. A common approximation for disk averaged spectra is to model a slant path with about 35° from nadir. The equivalent brightness spectra for the vertical and slant paths differ by less than 2 K in the center of the TIR-LW band (sensitive to the mid atmosphere) with somewhat larger differences for $\nu > 700\text{ cm}^{-1}$. On the other hand, the peak altitudes of the weighting functions are shifted downwards by some 10 km (see Fig. 1 lower left panel). As a consequence, the magnitude of the retrieved temperature will not change significantly, but the associated altitudes could change by several kilometers. It is also important to note that the preliminary constraints discussed in subsection 3.1 are independent of the viewing angle.

4.6 Auxiliary data, initial guess and a priori

For the solution of “real world” inverse problems a large variety of auxiliary data are required, e.g. instrument parameters or observation geometry. In the case of atmospheric IR spectroscopy these auxiliary data also comprise molecular optical properties (e.g. line lists or k-distributions); for temperature sounding these data also include pressure and molecular concentrations. These auxiliary data are often denoted “a priori”.

However, for optimal estimation (Rodgers 1976, 2000) this solely refers to the knowledge of the unknown state vector (e.g. temperature) prior to any measurement (all other auxiliary parameters are treated as “model parameters”). OE provides an estimate close to the a priori state vector where the relative weight of observation and a priori is determined by the respective measurement and a priori covariance matrices. (Note that this weighting is independent of the weighting function $\partial\mathcal{T}/\partial z$ defined in subsection 2.1.) Obviously a priori knowledge of exoplanetary atmospheric properties is scarce (see e.g. Shulyak et al. 2019 for a thorough discussion). Barstow (2020) noted that “the dependence of OE on an informative prior means that it is less appropriate for exoplanets”, which motivated the upgrade of the NEMESIS code (Irwin et al. 2008) with MultiNest (Feroz et al. 2009). Monte Carlo type retrievals are less sensitive to a priori, but for robust retrievals thousands to millions of time

³ <https://hitran.org/docs/iso-meta/>

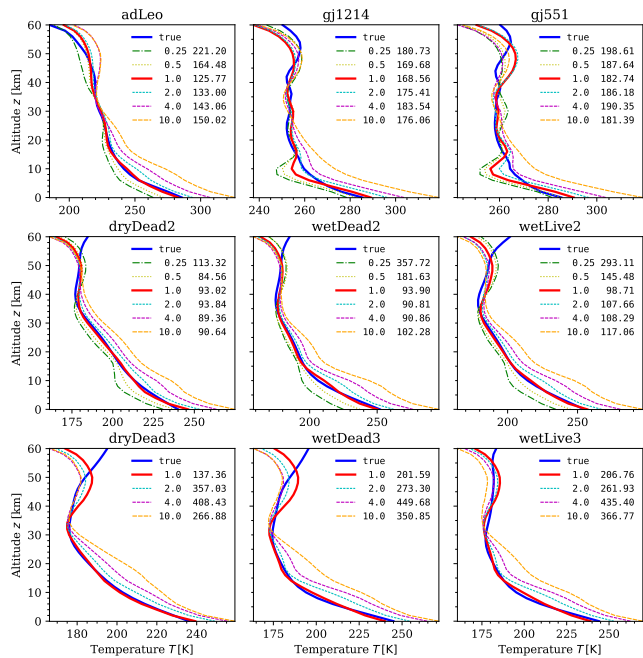


Figure 19. Impact of CO₂ concentration. MLS initial temperature, SVD “extrapolation” with 4 base vectors, $S/N = 20$, TIR-LW (M-Earths) or TIR-LWX (Trappist-1e) with Gaussian 0.25 cm^{-1} . The legend indicates the factor used to scale the CO₂ VMR isoprofile of the model atmosphere and the radiance residual norm.

expensive forward model evaluations are required (Fortney et al. 2021).

Some prior idea of the atmospheric state is required for Chahine-type inversions to compute the weighting functions and the total atmospheric transmission attenuating the surface emission (cf. Eqs. (1) and (5), (6)). However, our simulations have demonstrated that the inferred M-Earth temperatures are largely independent of the assumed Earth atmospheric model and/or initial guess temperature profile.

Parameterisations as proposed by Madhusudhan & Seager (2009); von Paris et al. (2013); Morley et al. (2017a) or Fossati et al. (2020) are frequently used for temperature retrievals (for a detailed discussion see Section 3 of Barstow & Heng 2020). Obviously, these parameterisations are motivated by physical insight and can also be considered as a kind of a priori knowledge.

For the iterative solution of nonlinear inverse problems by least squares (e.g. Schreier et al. 2020), OE (e.g. Irwin et al. 2008) (technically a constrained least squares) or Chahine relaxation, an initial guess is mandatory. For the Earth-like exoplanets considered here a climatological Earth temperature profile or an isoprofile defined by the mean of the observed EBT can be used to start the iteration. Alternatively, an atmospheric characterisation resulting from coupled photochemistry-climate codes such as 1D-TERRA (Wunderlich et al. 2020) can be used.

4.7 Atmospheric composition

Thermal emission IR spectra are sensitive to temperature but provide little information on atmospheric (molecular) composition. However these data are mandatory for radiative transfer modeling. In particular knowledge of the CO₂ concentration is important for temperature sounding exploiting its strong TIR-LW and TIR-SW bands. Actually

the concentrations of all molecules absorbing in the spectral region to be analysed are required: in the case of the two TIR bands, H₂O, ozone (O₃, longwave only) and methane (CH₄, shortwave) absorption are relevant. Note that H₂O does not have a large impact on the TIR-LW weighting functions.

Assuming CO₂ concentrations which are too low or too high likely has an impact on the quality of the retrievals. Further test runs have been performed with a setup similar to Fig. 17, but with CO₂ isoprofiles scaled by factors from 0.25 up to 10 in the model atmosphere. Figure 19 demonstrates that in most cases the residual norm is larger for incorrect CO₂ mixing ratios; in some cases the iteration fails (e.g. for the 0.1% CO₂ Trappist-1e atmospheres, usually because of negative temperatures), the number of iterations becomes larger, or the temperature profile shows stronger oscillations (zigzag profiles are unrealistic because the observed radiance is an integral (1) that is insensitive to small-scale “perturbations” of temperature and/or molecular densities).

An independent estimate of concentrations is therefore desirable. Carbon dioxide has several strong bands throughout the IR: in addition to the TIR bands there are further strong rotation-vibration bands in the shortwave and near IR (SWIR, NIR) at $2.7 \mu\text{m}$, $2.0 \mu\text{m}$, and $1.6 \mu\text{m}$. In fact the NIR bands as well as the TIR-SW band enabled the identification of CO₂ in the atmosphere of the Saturn-mass exoplanet WASP-39b with various JWST instruments (Ahler et al. 2023; Alderson et al. 2023; Rustamkulov et al. 2023) and the latter two SWIR bands are used operationally for monitoring of Earth’s CO₂ budget by several satellite missions such as OCO-2/3 or GOSAT (Crisp et al. 2004; Kuze et al. 2009). Regarding exoplanets the analysis of effective height / transit depth spectra provided by primary transit observations is therefore valuable. Moreover, the ratio of observed signals in two appropriate filter bands is a sensitive indicator of CO₂ atmospheric concentration (Rieke et al. 2015). For the joint analysis of primary and secondary transits see also Griffith (2014).

5 SUMMARY AND CONCLUSIONS

Temperature profiles of Earth-like exoplanets orbiting M-dwarfs have been retrieved from synthetic thermal IR emission spectra using Chahine-type relaxation methods along with a line-by-line radiative transfer code. The essential assumption is that for a particular wavenumber the outgoing radiation arises from a corresponding, well-defined altitude: In the band centre absorption is strong and only radiation from the upper atmosphere will be seen remotely; in the band wings absorption is weak and even photons from the lower atmosphere can traverse the entire atmosphere to the ToA and beyond. The feasibility of this method has been demonstrated using synthetic noise-contaminated observations of various Earth-like planets with N₂-O₂ dominated atmospheres orbiting M-dwarfs and for Trappist-1e planets of different surface conditions (wet/dry and dead/alive) and different carbon dioxide concentrations up to about 50%. (Note that the assumption of N₂-O₂ dominance is questionable for the high CO₂ Trappist-1e scenarios.)

The equivalent brightness temperature (EBT) spectrum corresponding to the observed intensity can be used to deliver temperature estimates extremely quickly: The minimum and maximum EBT values provide first constraints on the range of atmospheric temperatures independent of any a priori knowledge. The EBT in the carbon dioxide absorption bands can be readily “translated” (within seconds) to mid atmospheric temperatures. Using a handful of manually selected data points is problematic because of the noise, hence averaging of some neighboring spectral pixels is required (cf. Fig. 5). How-

ever, exploiting the entire intensity spectrum and the corresponding wavenumber-altitude mapping, as defined by the weighting functions, is preferably and clearly advantageous (Fig. 7). Furthermore, using both TIR-LW and TIR-SW data can be helpful to overcome the limited altitude sensitivity range of one region alone (Fig. 12). In any case, the quality of this guess is however related to an appropriate knowledge of the CO₂ concentrations, in particular in the case of the CO₂-rich Trappist-1e planets.

Iterative relaxation allows a refinement of the first guess, however, the success of the improvement relies on the inter/extrapolation used to complete the limited set of T data. Note that an update of the temperature will change cross sections, transmission, and weighting functions and hence also the wavenumber-altitude mapping.

Compared to classical nonlinear least squares fitting a clear advantage of the Chahine relaxation (or the related Smith and Twomey schemes) is the fact that no Jacobian (derivatives of the intensity I w.r.t. to the state vector elements) are required. This is clearly beneficial when finite differences are used to approximate the Jacobian as for (nonlinear) optimal estimation or in the SVEEEETIES study (Schreier et al. 2020) using Py4CATS (GARLIC exploits algorithmic differentiation, where the overhead for temperature Jacobians is only about a factor 2, see Schreier et al. (2015)). On the other hand, the time required for nonlinear least squares fitting (proportional to the number of iterations) can be reduced if a good initial guess is provided. Of course the “Chahine first guess” can be used as initial guess for any other iterative optimisation solver.

In conclusion, we have used an extension of the classical Chahine approach in an exoplanet context for the first time to our knowledge. This approach can deliver stable and reasonable temperature estimates for terrestrial-type exoplanets quickly (first guess in seconds, iterative refinements in minutes), even for challenging cases such as atmospheres with weak inversions and large CO₂ abundances. It is also attractive in view of the growing awareness on the “carbon footprint of large scale computing” and green computing (e.g. Jahnke et al. 2020). Hence it allows interesting new insight and provides a valuable addition to existing methods.

ACKNOWLEDGEMENTS

This foundations for this research were the DFG projects SCHR 1125/3-1, RA-714/7-1, and RA 714/9-1. We acknowledge the support of the DFG priority programme SPP 1992 “Exploring the Diversity of Extrasolar Planets (GO 2610/2-1)”. J.L.G. thanks ISSI Team 464 for useful discussion. We thank the German Research Foundation (DFG) for financial support via the project The Influence of Cosmic Rays on Exoplanetary Atmospheric Biosignatures (Project number 282759267). Finally we would like to thank Joanna Barstow for the constructive review.

DATA AVAILABILITY

Atmospheric data have been taken from Wunderlich et al. (2019, 2020) and molecular spectroscopy data have been obtained from HITRAN (<https://hitran.org/>); the data analysis software is an extension of the Py4CATS package (Schreier et al. 2019) available at <https://atmos.eoc.dlr.de/tools/Py4CATS/>.

REFERENCES

Ahrer E.-M., et al., 2023, *Nature*, 614, 649

- Alderson L., et al., 2023, *Nature*, 614, 664
- Anderson G., Clough S., Kneizys F., Chetwynd J., Shettle E., 1986, Technical Report TR-86-0110, AFGL Atmospheric Constituent Profiles (0 – 120 km). AFGL, Hanscom AFB, MA, USA
- Barstow J. K., 2020, *MNRAS*, 497, 4183
- Barstow J., Heng K., 2020, *Space Sci. Rev.*, 216, 82
- Barstow J., Irwin P., 2016, *MNRAS Letters*, 461, L92
- Barstow J., Aigrain S., Irwin P., Fletcher L., Lee J.-M., 2013, *MNRAS*, 434, 2616
- Barstow J. K., Aigrain S., Irwin P. G. J., Kendrew S., Fletcher L. N., 2016, *MNRAS*, 458, 2657
- Barstow J., Changeat Q., Garland R., Line M., Rocchetto M., Waldmann I., 2020, *MNRAS*, 493, 4884
- Barstow J., Changeat Q., Chubb K. L., Cubillos P. E., Edwards B., MacDonald R. J., Min M., Waldmann I., 2022, *Exp. Astron.*, 53, 447
- Benz W., Ehrenreich D., Isaak K., 2018, in Deeg H., Belmonte J., eds., *Handbook of Exoplanets*. Springer, doi:10.1007/978-3-319-55333-7_84
- Bernath P., 2017, *JQSRT*, 186, 3
- Blecic J., Dobbs-Dixon I., Greene T., 2017, *APJ*, 848, 127
- Caldas A., Leconte J., Selsis F., Waldmann I. P., Bordé P., Rocchetto M., Charnay B., 2019, *A & A*, 623, A161
- Chahine M., 1968, *J. Opt. Soc. Am.*, 58, 1634
- Chahine M., 1970, *J. Atmos. Sci.*, 27, 960
- Chahine M., 1972, *J. Atmos. Sci.*, 29, 741
- Chahine M., et al., 2006, *Bull. Am. Met. Soc.*, 87, 911
- Clough S., Kneizys F., Davies R., 1989, *Atm. Res.*, 23, 229
- Crisp D., et al., 2004, *Adv. Space Res.*, 34, 700
- Cubillos P. E., Blecic J., 2021, *MNRAS*, 505, 2675
- Defrère D., et al., 2018, *Exp. Astron.*, 46, 543
- Dennis, Jr. J., Gay D., Welsch R., 1981a, *ACM Trans. Math. Soft.*, 7, 348
- Dennis, Jr. J., Gay D., Welsch R., 1981b, *ACM Trans. Math. Soft.*, 7, 369
- Faucher T. J., et al., 2020, *Geosci. Model Dev.*, 13, 707
- Feng Y., Line M., Fortney J., Stevenson K., Bean J., Kreidberg L., Parmentier V., 2016, *APJ*, 829, 52
- Feroz F., Hobson M. P., Bridges M., 2009, *MNRAS*, 398, 1601
- Fortney J. J., Barstow J. K., Madhusudhan N., 2021, Atmospheric Modelling and Retrieval ([arXiv:2109.01976](https://arxiv.org/abs/2109.01976))
- Fossati L., et al., 2020, *A & A*, 643, A131
- Garand L., et al., 2001, *JGR*, 106, 24017
- Gautier D., Lacombe A., Revah I., 1977, *J. Atmos. Sci.*, 34, 1130
- Gautier D., Marten A., Baluteau J. P., Lacombe A., 1979, *Icarus*, 37, 214
- Gebauer S., Grenfell J., Lehmann R., Rauer H., 2018, *ACS Earth Space Chem.*, 2, 1112
- Gillon M., et al., 2017, *Nature*, 542, 456
- Goody R., Yung Y., 1989, *Atmospheric Radiation — Theoretical Basis*, second edn. Oxford University Press
- Gordon I., et al., 2017, *JQSRT*, 203, 3
- Gordon I., et al., 2022, *JQSRT*, 277, 107949
- Greene T. P., Line M. R., Montero C., Fortney J. J., Lustig-Yaeger J., Luther K., 2016, *APJ*, 817, 17
- Griffith C. A., 2014, *Philos. Trans. Roy. Soc. London, Ser. A*, 372, 20130086
- Grimm S. L., et al., 2018, *A & A*, 613, A68
- Hanel R., Conrath B., Jennings D., Samuelson R., 2003, *Exploration of the Solar System by Infrared Remote Sensing*, 2 edn. Cambridge University Press
- Harris C., et al., 2020, *Nature*, 585, 357
- Haus R., Titov D., 2000, *PSS*, 48, 473
- Hilton F., et al., 2012, *Bull. Am. Met. Soc.*, 93, 347
- Hunter J., 2007, *Comp. Sci. & Eng.*, 9, 90

- Irwin P., et al., 2008, *JQSRT*, 109, 1136
- Jahnke K., et al., 2020, *Nat. Astron.*, 4, 812
- Karman T., et al., 2019, *Icarus*, 328, 160
- Konrad B. S., et al., 2022, *A & A*, 664, A23
- Krissansen-Totton J., Fortney J. J., 2022, *APJ*, 933, 115
- Krissansen-Totton J., Garland R., Irwin P., Catling D., 2018, *AJ*, 156, 114
- Kuze A., Suto H., Nakajima M., Hamazaki T., 2009, *Appl. Opt.*, 48, 6716
- Lee J.-M., Fletcher L., Irwin P., 2012, *MNRAS*, 420, 170
- Lellouch E., Encrenaz T., Phillips T., Falgarone E., Billebaud F., 1991a, *PSS*, 39, 209
- Lellouch E., Paubert G., Encrenaz T., 1991b, *PSS*, 39, 219
- Line M., Zhang X., Vasisht G., Natraj V., Chen P., Yung Y., 2012, *APJ*, 749, 93
- Line M. R., et al., 2013, *APJ*, 775, 137
- Liou K.-N., 1980, *An Introduction to Atmospheric Radiation*. Academic Press, Orlando
- Lustig-Yaeger J., Meadows V., Lincowski A., 2019, *AJ*, 158, 27
- MacDonald R. J., Batalha N. E., 2023, *Res. Notes AAS*, 7, 54
- MacDonald R., Madhusudhan N., 2017, *MNRAS*, 469, 1979
- MacDonald R. J., Goyal J. M., Lewis N. K., 2020, *APJ*, 893, L43
- Madhusudhan N., 2018, in Deeg H., Belmonte J., eds., *Handbook of Exoplanets*. Springer, doi:10.1007/978-3-319-30648-3_104-1
- Madhusudhan N., Seager S., 2009, *APJ*, 707, 24
- Mayor M., Queloz D., 1995, *Nature*, 378, 355
- Menzel W. P., Schmit T. J., Zhang P., Li J., 2018, *Bull. Am. Met. Soc.*, 99, 583
- Mérand A., et al., 2021, *The Messenger*, 184, 8
- Mikal-Evans T., 2021, *MNRAS*, 510, 980
- Min M., Ormel C. W., Chubb K., Helling C., Kawashima Y., 2020, *A & A*, 642, A28
- More J., 1978, in Watson G., ed., *Numerical Analysis*. Springer, Lecture Notes in Mathematics 630
- Morley C., Knutson H., Line M., Fortney J., Thorngren D., Marley M. S., Teal D., Lupu R., 2017a, *AJ*, 153, 86
- Morley C., Kreidberg L., Rustamkulov Z., Robinson T., Fortney J., 2017b, *APJ*, 850, 121
- Parmentier V., Guillot T., 2014, *A & A*, 562, A133
- Pluriel W., 2023, *Remote Sens.*, 15, 635
- Quanz S., et al., 2022a, *Exp. Astron.*
- Quanz S. P., et al., 2022b, *A & A*, 664, A21
- Rauer H., Catala C., et al., 2014, *Exp. Astron.*, 38, 249
- Richard C., et al., 2012, *JQSRT*, 113, 1276
- Rieke G. H., et al., 2015, *PASP*, 127, 584
- Rodgers C., 1976, *Rev. Geophys. Space Phys.*, 14, 609
- Rodgers C., 2000, *Inverse Methods for Atmospheric Sounding: Theory and Practise*. World Scientific, Singapore
- Rothman L., et al., 1987, *Appl. Opt.*, 26, 4058
- Rustamkulov Z., et al., 2023, *Nature*, 614, 659
- Schreier F., 2018, *MNRAS*, 479, 3068
- Schreier F., Gimeno García S., Hedelt P., Hess M., Mendrok J., Vasquez M., Xu J., 2014, *JQSRT*, 137, 29
- Schreier F., Gimeno García S., Vasquez M., Xu J., 2015, *JQSRT*, 164, 147
- Schreier F., Städt S., Hedelt P., Godolt M., 2018a, *Molec. Astrophys.*, 11, 1
- Schreier F., Milz M., Buehler S., von Clarman T., 2018b, *JQSRT*, 211, 64
- Schreier F., Gimeno García S., Hochstaffl P., Städt S., 2019, *Atmosphere*, 10, 262
- Schreier F., Städt S., Wunderlich F., Godolt M., Grenfell J., 2020, *A & A*, 633, A156
- Shine K., Ptashnik I., Rädcl G., 2012, *Surv. Geophys.*, 33, 535
- Shulyak D., Rengel M., Reiners A., Seemann U., Yan F., 2019, *A & A*, 629, A109
- Smith W., 1970, *Appl. Opt.*, 9, 1993
- Taylor F., et al., 1980, *JGR*, 85, 7963
- Taylor J., Parmentier V., Irwin P., Aigrain S., Lee G., Krissansen-Totton J., 2020, *MNRAS*, 493, 4342
- Tinetti G., et al., 2018, *Exp. Astron.*, 46, 135
- Twomey S., Herman B., Rabinoff R., 1977, *J. Atmos. Sci.*, 34, 1085
- Virtanen P., et al., 2020, *Nature Methods*, 17, 261
- Waldmann I., Tinetti G., Rocchetto M., Barton E., Yurchenko S., Tennyson J., 2015, *APJ*, 802
- Wunderlich F., et al., 2019, *A & A*, 624, A49
- Wunderlich F., et al., 2020, *APJ*, 901, 126
- Zdunkowski W., Trautmann T., Bott A., 2007, *Radiation in the Atmosphere — A Course in Theoretical Meteorology*. Cambridge University Press
- van der Walt S., Colbert S., Varoquaux G., 2011, *Comp. Sci. & Eng.*, 13, 22
- von Paris P., Hedelt P., Schreier F., Trautmann T., 2013, *A & A*, 551, A120

This paper has been typeset from a $\text{\TeX}/\text{\LaTeX}$ file prepared by the author.